



Search for Continuous and Transient Neutrino Emission Associated with IceCube's Highest-energy Tracks: An 11 yr Analysis

Downloaded from: <https://research.chalmers.se>, 2024-04-18 14:50 UTC

Citation for the original published paper (version of record):





Abbasi, R., Ackermann, M., Adams, J. et al (2024). Search for Continuous and Transient Neutrino Emission Associated with IceCube's Highest-energy Tracks: An 11 yr Analysis. *Astrophysical Journal*, 964(1).
<http://dx.doi.org/10.3847/1538-4357/ad18d6>

N.B. When citing this work, cite the original published paper.



Search for Continuous and Transient Neutrino Emission Associated with IceCube's Highest-energy Tracks: An 11 yr Analysis

R. Abbasi¹, M. Ackermann², J. Adams³, S. K. Agarwalla^{4,64}, J. A. Aguilar⁵, M. Ahlers⁶, J. M. Alameddine⁷, N. M. Amin⁸, K. Andeen⁹, G. Anton¹⁰, C. Argüelles¹¹, Y. Ashida¹², S. Athanasiadou², S. N. Axani⁸, X. Bai¹³, A. Balagopal V.⁴, M. Baricevic⁴, S. W. Barwick¹⁴, V. Basu⁴, R. Bay¹⁵, J. J. Beatty^{16,17}, J. Becker Tjus^{18,65}, J. Beise¹⁹, C. Bellenghi²⁰, C. Benning²¹, S. BenZvi²², D. Berley²³, E. Bernardini²⁴, D. Z. Besson²⁵, E. Blaufuss²³, S. Blot², F. Bontempo²⁶, J. Y. Book¹¹, C. Boscolo Meneguolo²⁴, S. Böser²⁷, O. Botner¹⁹, J. Böttcher²¹, E. Bourbeau⁶, J. Braun⁴, B. Brinson²⁸, J. Brostean-Kaiser², R. T. Burley²⁹, R. S. Busse³⁰, D. Butterfield⁴, M. A. Campana³¹, K. Carloni¹¹, E. G. Carnie-Bronca²⁹, S. Chattopadhyay^{4,64}, N. Chau⁵, C. Chen²⁸, Z. Chen³², D. Chirkin⁴, S. Choi³³, B. A. Clark²³, S. Coenders²⁰, A. Coleman¹⁹, G. H. Collin³⁴, A. Connolly^{16,17}, J. M. Conrad³⁴, P. Coppin³⁵, P. Correa³⁵, D. F. Cowen^{36,37}, P. Dave²⁸, C. De Clercq³⁵, J. J. DeLaunay³⁸, D. Delgado¹¹, S. Deng²¹, K. Deoskar³⁹, A. Desai⁴, P. Desiati⁴, K. D. de Vries³⁵, G. de Wasseige⁴⁰, T. DeYoung⁴¹, A. Diaz³⁴, J. C. Díaz-Vélez⁴, M. Dittmer³⁰, A. Domi¹⁰, H. Dujmovic⁴, M. A. DuVernois⁴, T. Ehrhardt²⁷, A. Eimer¹⁰, P. Eller²⁰, E. Ellinger⁴², S. El Mentawi²¹, D. Elsässer⁷, R. Engel^{26,43}, H. Erpenbeck⁴, J. Evans²³, P. A. Evenson⁸, K. L. Fan²³, K. Fang⁴, K. Farrag⁴⁴, A. R. Fazely⁴⁵, A. Fedynitch⁴⁶, N. Feigl⁴⁷, S. Fiedlschuster¹⁰, C. Finley³⁹, L. Fischer², D. Fox³⁶, A. Franckowiak¹⁸, A. Fritz²⁷, P. Fürst²¹, J. Gallagher⁴⁸, E. Ganster²¹, A. Garcia¹¹, L. Gerhardt⁴⁹, A. Ghadimi³⁸, C. Glaser¹⁹, T. Glauch²⁰, T. Glüsenskamp^{10,19}, N. Goehke⁴³, J. G. Gonzalez⁸, S. Goswami³⁸, D. Grant⁴¹, S. J. Gray²³, O. Gries²¹, S. Griffin⁴, S. Griswold²², K. M. Groth⁶, C. Günther²¹, P. Gutjahr⁷, C. Haack¹⁰, A. Hallgren¹⁹, R. Halliday⁴¹, L. Halve²¹, F. Halzen⁴, H. Hamdaoui³², M. Ha Minh²⁰, K. Hanson⁴, J. Hardin³⁴, A. A. Harnisch⁴¹, P. Hatch⁵⁰, A. Haungs²⁶, K. Helbing⁴², J. Hellrung¹⁸, F. Henningsen²⁰, L. Heuermann²¹, N. Heyer¹⁹, S. Hickford⁴², A. Hidvegi³⁹, C. Hill⁴⁴, G. C. Hill²⁹, K. D. Hoffman²³, S. Hori⁴, K. Hoshina^{4,66}, W. Hou²⁶, T. Huber²⁶, K. Hultqvist³⁹, M. Hünnefeld⁷, R. Hussain⁴, K. Hymon⁷, S. In³³, A. Ishihara⁴⁴, M. Jacquart⁴, O. Janik²¹, M. Jansson³⁹, G. S. Japaridze⁵¹, M. Jeong¹², M. Jin¹¹, B. J. P. Jones⁵², N. Kamp¹¹, D. Kang²⁶, W. Kang³³, X. Kang³¹, A. Kappes³⁰, D. Kappesser²⁷, L. Kardum⁷, T. Karg², M. Karl²⁰, A. Karle⁴, A. Katil⁵³, U. Katz¹⁰, M. Kauer⁴, J. L. Kelley⁴, A. Khatee Zathul⁴, A. Kheirandish^{54,55}, J. Kiryluk³², S. R. Klein^{15,49}, A. Kochocki⁴¹, R. Koirala⁸, H. Kolanoski⁴⁷, T. Kontrimas²⁰, L. Köpke²⁷, C. Kopper¹⁰, D. J. Koskinen⁶, P. Koundal²⁶, M. Kovacevich³¹, M. Kowalski^{2,47}, T. Kozynets⁶, J. Krishnamoorthi^{4,64}, K. Kruiswijk⁴⁰, E. Krupczak⁴¹, A. Kumar², E. Kun¹⁸, N. Kurahashi³¹, N. Lad², C. Lagunas Gualda², M. Lamoureux⁴⁰, M. J. Larson²³, S. Latseva²¹, F. Lauber⁴², J. P. Lazar^{4,11}, J. W. Lee³³, K. Leonard DeHolton³⁷, A. Leszczyńska⁸, M. Lincetto¹⁸, Q. R. Liu⁴, M. Liubarska⁵³, E. Lohfink²⁷, C. Love³¹, C. J. Lozano Mariscal³⁰, L. Lu⁴, F. Lucarelli⁵⁶, W. Luszczak^{16,17}, Y. Lyu^{15,49}, J. Madsen⁴, K. B. M. Mahn⁴¹, Y. Makino⁴, E. Manao²⁰, S. Mancina^{4,24}, W. Marie Sainte⁴, I. C. Mariş⁵, S. Marka⁵⁷, Z. Marka⁵⁷, M. Marsee³⁸, I. Martinez-Soler¹¹, R. Maruyama⁵⁸, F. Mayhew⁴¹, T. McElroy⁵³, F. McNally⁵⁹, J. V. Mead⁶, K. Meagher⁴, S. Mechbal², A. Medina¹⁷, M. Meier⁴⁴, Y. Merckx³⁵, L. Merten¹⁸, J. Micallef⁴¹, J. Mitchell⁴⁵, T. Montaruli⁵⁶, R. W. Moore⁵³, Y. Morii⁴⁴, R. Morse⁴, M. Moulai⁴, T. Mukherjee²⁶, R. Naab², R. Nagai⁴⁴, M. Nakos⁴, U. Naumann⁴², J. Necker², A. Negi⁵², M. Neumann³⁰, H. Niederhausen⁴¹, M. U. Nisa⁴¹, A. Noell²¹, A. Novikov⁸, S. C. Nowicki⁴¹, A. Obertacke Pollmann⁴⁴, V. O'Dell⁴, M. Oehler²⁶, B. Oeyen⁶⁰, A. Olivas²³, R. Orsoe²⁰, J. Osborn⁴, E. O'Sullivan¹⁹, H. Pandya⁸, N. Park⁵⁰, G. K. Parker⁵², E. N. Paudel⁸, L. Paul¹³, C. Pérez de los Heros¹⁹, J. Peterson⁴, S. Philippen²¹, A. Pizzuto⁴, M. Plum¹³, A. Pontén¹⁹, Y. Popovych²⁷, M. Prado Rodriguez⁴, B. Pries⁴¹, R. Procter-Murphy²³, G. T. Przybylski⁴⁹, C. Raab⁴⁰, J. Rack-Helleis²⁷, K. Rawlins⁶¹, Z. Rechav⁴, A. Rehman⁸, P. Reichherzer¹⁸, G. Renzi⁵, E. Resconi²⁰, S. Reusch², W. Rhode⁷, B. Riedel⁴, A. Rifaie²¹, E. J. Roberts²⁹, S. Robertson^{15,49}, S. Rodan³³, G. Roellinghoff³³, M. Rongen¹⁰, C. Rott^{12,33}, T. Ruhe⁷, L. Ruohan²⁰, D. Ryckbosch⁶⁰, I. Safa^{4,11}, J. Saffer⁴³, D. Salazar-Gallegos⁴¹, P. Sampathkumar²⁶, S. E. Sanchez Herrera⁴¹, A. Sandrock⁴², M. Santander³⁸, S. Sarkar⁵³, S. Sarkar⁶², J. Savelberg²¹, P. Savina⁴, M. Schaufel²¹, H. Schieler²⁶, S. Schindler¹⁰, L. Schlickmann²¹, B. Schlüter³⁰, F. Schlüter⁵, N. Schmeisser⁴², T. Schmidt²³, J. Schneider¹⁰, F. G. Schröder^{8,26}, L. Schumacher¹⁰, G. Schwefer²¹, S. Sclafani²³, D. Seckel⁸, M. Seikh²⁵, S. Seunarine⁶³, R. Shah³¹, S. Shefali⁴³, N. Shimizu⁴⁴, M. Silva⁴, B. Skrzypek¹¹, B. Smithers⁵², R. Snihur⁴, J. Soedingrekso⁷, A. Søgaard⁶, D. Soldin⁴³, P. Soldin²¹, G. Sommani¹⁸, C. Spannfellner²⁰, G. M. Spiczak⁶³, C. Spiering², M. Stamatikos¹⁷, T. Stanev⁸, T. Stezelberger⁴⁹, T. Stürwald⁴², T. Stuttard⁶, G. W. Sullivan²³, I. Taboada²⁸, S. Ter-Antonyan⁴⁵, M. Thiesmeyer²¹, W. G. Thompson¹¹, J. Thwaites⁴, S. Tilav⁸, K. Tollefson⁴¹, C. Tönnis³³, S. Toscano⁵, D. Tosi⁴, A. Trettin², C. F. Tung²⁸, R. Turcotte²⁶, J. P. Twagirayezu⁴¹, M. A. Unland Elorrieta³⁰, A. K. Upadhyay^{4,64}, K. Upshaw⁴⁵, A. Vaidyanathan⁹, N. Valtonen-Mattila¹⁹, J. Vandenbroucke⁴, N. van Eijndhoven³⁵, D. Vannerom³⁴, J. van Santen², J. Vara³⁰, J. Veitch-Michaelis⁴, M. Venugopal²⁶, M. Vereecken⁴⁰, S. Verpoest⁸, D. Veske⁵⁷, A. Vijai²³, C. Walck³⁹, C. Weaver⁴¹, P. Weigel³⁴, A. Weindl²⁶, J. Weldert³⁷, A. Y. Wen¹¹, C. Wendt⁴, J. Werthebach⁷, M. Weyrauch²⁶, N. Whitehorn⁴¹, C. H. Wiebusch²¹, D. R. Williams³⁸

L. Witthaus⁷, A. Wolf²¹, M. Wolf²⁰ , G. Wrede¹⁰, X. W. Xu⁴⁵, J. P. Yanez⁵³, E. Yildizci⁴, S. Yoshida⁴⁴ , R. Young²⁵, S. Yu⁴¹,
T. Yuan⁴ , Z. Zhang³² , P. Zhelnin¹¹, P. Zilberman⁴, and M. Zimmerman⁴

IceCube Collaboration

- ¹ Department of Physics, Loyola University Chicago, Chicago, IL 60660, USA; analysis@icecube.wisc.edu
- ² Deutsches Elektronen-Synchrotron DESY, Platanenallee 6, D-15738 Zeuthen, Germany
- ³ Department of Physics and Astronomy, University of Canterbury, Private Bag 4800, Christchurch, New Zealand
- ⁴ Department of Physics and Wisconsin IceCube Particle Astrophysics Center, University of Wisconsin–Madison, Madison, WI 53706, USA
- ⁵ Université Libre de Bruxelles, Science Faculty CP230, B-1050 Brussels, Belgium
- ⁶ Niels Bohr Institute, University of Copenhagen, DK-2100 Copenhagen, Denmark
- ⁷ Department of Physics, TU Dortmund University, D-44221 Dortmund, Germany
- ⁸ Bartol Research Institute and Department of Physics and Astronomy, University of Delaware, Newark, DE 19716, USA
- ⁹ Department of Physics, Marquette University, Milwaukee, WI 53201, USA
- ¹⁰ Erlangen Centre for Astroparticle Physics, Friedrich-Alexander-Universität Erlangen-Nürnberg, D-91058 Erlangen, Germany
- ¹¹ Department of Physics and Laboratory for Particle Physics and Cosmology, Harvard University, Cambridge, MA 02138, USA
- ¹² Department of Physics and Astronomy, University of Utah, Salt Lake City, UT 84112, USA
- ¹³ Physics Department, South Dakota School of Mines and Technology, Rapid City, SD 57701, USA
- ¹⁴ Department of Physics and Astronomy, University of California, Irvine, CA 92697, USA
- ¹⁵ Department of Physics, University of California, Berkeley, CA 94720, USA
- ¹⁶ Department of Astronomy, Ohio State University, Columbus, OH 43210, USA
- ¹⁷ Department of Physics and Center for Cosmology and Astro-Particle Physics, Ohio State University, Columbus, OH 43210, USA
- ¹⁸ Fakultät für Physik & Astronomie, Ruhr-Universität Bochum, D-44780 Bochum, Germany
- ¹⁹ Department of Physics and Astronomy, Uppsala University, Box 516, SE-75120 Uppsala, Sweden
- ²⁰ Physik-department, Technische Universität München, D-85748 Garching, Germany
- ²¹ III. Physikalisches Institut, RWTH Aachen University, D-52056 Aachen, Germany
- ²² Department of Physics and Astronomy, University of Rochester, Rochester, NY 14627, USA
- ²³ Department of Physics, University of Maryland, College Park, MD 20742, USA
- ²⁴ Dipartimento di Fisica e Astronomia Galileo Galilei, Università Degli Studi di Padova, I-35122 Padova PD, Italy
- ²⁵ Department of Physics and Astronomy, University of Kansas, Lawrence, KS 66045, USA
- ²⁶ Karlsruhe Institute of Technology, Institute for Astroparticle Physics, D-76021 Karlsruhe, Germany
- ²⁷ Institute of Physics, University of Mainz, Staudinger Weg 7, D-55099 Mainz, Germany
- ²⁸ School of Physics and Center for Relativistic Astrophysics, Georgia Institute of Technology, Atlanta, GA 30332, USA
- ²⁹ Department of Physics, University of Adelaide, Adelaide, 5005, Australia
- ³⁰ Institut für Kernphysik, Westfälische Wilhelms-Universität Münster, D-48149 Münster, Germany
- ³¹ Department of Physics, Drexel University, 3141 Chestnut Street, Philadelphia, PA 19104, USA
- ³² Department of Physics and Astronomy, Stony Brook University, Stony Brook, NY 11794-3800, USA
- ³³ Department of Physics, Sungkyunkwan University, Suwon 16419, Republic of Korea
- ³⁴ Department of Physics, Massachusetts Institute of Technology, Cambridge, MA 02139, USA
- ³⁵ Vrije Universiteit Brussel (VUB), Dienst ELEM, B-1050 Brussels, Belgium
- ³⁶ Department of Astronomy and Astrophysics, Pennsylvania State University, University Park, PA 16802, USA
- ³⁷ Department of Physics, Pennsylvania State University, University Park, PA 16802, USA
- ³⁸ Department of Physics and Astronomy, University of Alabama, Tuscaloosa, AL 35487, USA
- ³⁹ Oskar Klein Centre and Department of Physics, Stockholm University, SE-10691 Stockholm, Sweden
- ⁴⁰ Centre for Cosmology, Particle Physics and Phenomenology—CP3, Université catholique de Louvain, Louvain-la-Neuve, Belgium
- ⁴¹ Department of Physics and Astronomy, Michigan State University, East Lansing, MI 48824, USA
- ⁴² Department of Physics, University of Wuppertal, D-42119 Wuppertal, Germany
- ⁴³ Karlsruhe Institute of Technology, Institute of Experimental Particle Physics, D-76021 Karlsruhe, Germany
- ⁴⁴ Department of Physics and The International Center for Hadron Astrophysics, Chiba University, Chiba 263-8522, Japan
- ⁴⁵ Department of Physics, Southern University, Baton Rouge, LA 70813, USA
- ⁴⁶ Institute of Physics, Academia Sinica, Taipei, 11529, Taiwan
- ⁴⁷ Institut für Physik, Humboldt-Universität zu Berlin, D-12489 Berlin, Germany
- ⁴⁸ Department of Astronomy, University of Wisconsin–Madison, Madison, WI 53706, USA
- ⁴⁹ Lawrence Berkeley National Laboratory, Berkeley, CA 94720, USA
- ⁵⁰ Department of Physics, Engineering Physics, and Astronomy, Queen’s University, Kingston, ON K7L 3N6, Canada
- ⁵¹ CTSPS, Clark-Atlanta University, Atlanta, GA 30314, USA
- ⁵² Department of Physics, University of Texas at Arlington, 502 Yates Street, Science Hall Room 108, Box 19059, Arlington, TX 76019, USA
- ⁵³ Department of Physics, University of Alberta, Edmonton, AB T6G 2E1, Canada
- ⁵⁴ Department of Physics & Astronomy, University of Nevada, Las Vegas, NV 89154, USA
- ⁵⁵ Nevada Center for Astrophysics, University of Nevada, Las Vegas, NV 89154, USA
- ⁵⁶ Département de physique nucléaire et corpusculaire, Université de Genève, CH-1211 Genève, Switzerland
- ⁵⁷ Columbia Astrophysics and Nevis Laboratories, Columbia University, New York, NY 10027, USA
- ⁵⁸ Department of Physics, Yale University, New Haven, CT 06520, USA
- ⁵⁹ Department of Physics, Mercer University, Macon, GA 31207-0001, USA
- ⁶⁰ Department of Physics and Astronomy, University of Gent, B-9000 Gent, Belgium
- ⁶¹ Department of Physics and Astronomy, University of Alaska Anchorage, 3211 Providence Drive, Anchorage, AK 99508, USA

⁶²Department of Physics, University of Oxford, Parks Road, Oxford OX1 3PU, UK⁶³Department of Physics, University of Wisconsin, River Falls, WI 54022, USA

Received 2023 September 21; revised 2023 December 13; accepted 2023 December 14; published 2024 March 13

Abstract

IceCube alert events are neutrinos with a moderate-to-high probability of having astrophysical origin. In this study, we analyze 11 yr of IceCube data and investigate 122 alert events and a selection of high-energy tracks detected between 2009 and the end of 2021. This high-energy event selection (alert events + high-energy tracks) has an average probability of ≥ 0.5 of being of astrophysical origin. We search for additional continuous and transient neutrino emission within the high-energy events' error regions. We find no evidence for significant continuous neutrino emission from any of the alert event directions. The only locally significant neutrino emission is the transient emission associated with the blazar TXS 0506+056, with a local significance of 3σ , which confirms previous IceCube studies. When correcting for 122 test positions, the global p -value is 0.156 and compatible with the background hypothesis. We constrain the total continuous flux emitted from all 122 test positions at 100 TeV to be below $1.2 \times 10^{-15} (\text{TeV cm}^2 \text{s})^{-1}$ at 90% confidence assuming an E^{-2} spectrum. This corresponds to 4.5% of IceCube's astrophysical diffuse flux. Overall, we find no indication that alert events in general are linked to lower-energy continuous or transient neutrino emission.

Unified Astronomy Thesaurus concepts: High energy astrophysics (739); Active galactic nuclei (16); Neutrino astronomy (1100); Transient sources (1851); Blazars (164)

1. Introduction

The IceCube Neutrino Observatory (Aartsen et al. 2017a) is a Cherenkov detector using a cubic kilometer of Antarctic ice at the geographic South Pole to primarily (but not exclusively) study high-energy astrophysical neutrinos. Its duty cycle is greater than 99% (Aartsen et al. 2017a), and its field of view covers the full sky while being most sensitive to high-energy neutrino events near the celestial equator. This makes IceCube ideal for surveying the sky (Aartsen et al. 2017b). As part of the real-time program, IceCube alerts other telescopes upon detection of a neutrino event with a high probability of being of astrophysical origin, which can then trigger follow-up observations (Kintscher 2016; Aartsen et al. 2017b; Blaufuss et al. 2019).

On 2017 September 22, IceCube detected a neutrino of likely astrophysical origin (IceCube-170922A⁶⁷). This triggered multiwavelength follow-up observations, which detected a flaring blazar (TXS 0506+056) at the reconstructed origin direction of IceCube-170922A (Aartsen et al. 2018a). This correlation is significant at a 3σ level (Aartsen et al. 2018a). Additionally, a neutrino flare was identified originating from the same direction between 2014 September and 2015 March with a significance of 3.5σ (Aartsen et al. 2018b).

This detection demonstrates that IceCube alerts can point to neutrino source candidates due to their high probability of being of astrophysical origin, and we aim to investigate the origin directions of other IceCube alerts. A preliminary search showed no indication of continuous neutrino emission (Karl 2019). However, the IceCube alert criteria have since been updated (Blaufuss et al. 2019; Abbasi et al. 2023a). The

IceCube data have also been reprocessed with improved calibration of the optical sensors (Aartsen et al. 2020; Abbasi et al. 2021a). This leads to improved energy and direction reconstruction compared to previous results in Aartsen et al. (2015, 2018b, 2020) and Abbasi et al. (2021b, 2021c, 2021d). A first analysis benefiting from this new processing (Abbasi et al. 2022a) detected the neutrino signal from the Seyfert II galaxy NGC 1068 with a significance of 4.2σ (compared to 2.9σ in Aartsen et al. 2020). A large part of the increase (0.9σ) is due to improved data processing and calibration. More details about effects on the data are discussed in Appendix B and the supplementary material of Abbasi et al. (2022a).

In this work, we analyze 11 yr of reprocessed IceCube data (throughgoing muon tracks; see Table 1) and search for an excess of neutrino-induced muons. We apply a conservative lower limit on the angular uncertainty of $0^\circ.2$, whereas the median angular resolution is $0^\circ.57$ (compared to a median angular resolution of $0^\circ.59$ before the reprocessing). We identify possible neutrino production sites by looking at the origin of high-energy neutrinos that have a high probability of being of astrophysical origin. IceCube's highest-energy neutrinos with the largest astrophysical purity are events from the new selection of IceCube alerts published in the so-called "gold" alert channel (Blaufuss et al. 2019; Abbasi et al. 2023a). Additionally, we extend the list by including 18 high-energy events from Abbasi et al. (2022b) that were confirmed to be likely astrophysical events by a new event classifier (Kronmueller & Glauch 2019). Since we use a combination of IceCube alert events and high-energy tracks identified retrospectively, we will refer to our event selection as "alert+ events" for brevity. All IceCube data used in this work (lower- and high-energy events) have been reprocessed.

In this work, we excluded alert+ events within 30° of the geographic poles (affecting three events), for which we have smaller statistics for the background. Other IceCube analyses have applied different decl. cuts (for example, including all events up to 81° decl., Abbasi et al. 2022a, or up to 82° , Aartsen et al. 2020). Additionally, we removed alert+ events with large uncertainties ($\geq 100c \text{ deg}^2$, affecting two events). As a result, our final sample consists of 122 high-energy events (104 IceCube alert events and 18 high-energy tracks, listed in Table 3), detected between 2009 and the end of 2021. On

⁶⁴ Also at Institute of Physics, Sachivalaya Marg, Sainik School Post, Bhubaneswar 751005, India.

⁶⁵ Also at Department of Space, Earth and Environment, Chalmers University of Technology, 412 96 Gothenburg, Sweden.

⁶⁶ Also at Earthquake Research Institute, University of Tokyo, Bunkyo, Tokyo 113-0032, Japan.

⁶⁷ https://gc.gsfc.nasa.gov/notices_amon/50579430_130033.amon



Table 1
Overview of the Improved and Reprocessed Data Samples in This Analysis

Year	Livetime (days)	Number of Events	Start	End
IC 59	353.578	107,011	2009 May 5	2010 May 31
IC 79	316.045	93,133	2010 Jun 1	2011 May 13
IC 86 2011–2019	3184.163	1,133,364	2011 May 13	2020 May 29

Note. The columns list the configuration of the detector (“IC” and the number of deployed strings), the uptime (livetime) of the detector in days, the number of events in each sample, and the start and end dates of the data subset.

average, our selected alert+ events have a probability of being astrophysical of $\gtrsim 0.5$. The probability of being astrophysical is spectrum-dependent and based on the muon neutrino spectrum measured by IceCube (Haack & Wiebusch 2017; Abbasi et al. 2022b). The median angular resolution (90% uncertainty regions) of alert+ events is $2^\circ.1$. In Figure 1, we show a map of all arrival directions and their 90% uncertainty regions of IceCube alert+ events investigated in this work. These events provide positions of interest analogous to a catalog of possible neutrino sources. Since IceCube alert+ events trigger this analysis, we remove the respective alert+ event from the 11 yr of IceCube data when running the analysis. We present the analysis method in Section 2 and the results in Section 3.

2. Analysis Method

We use an unbinned likelihood approach as presented by Braun et al. (2008). In this work, we investigate two source types: continuous sources and transient sources. We compare two hypotheses (each with a set of parameters θ).

1. *Background hypothesis* $H_0(\theta_0)$. The background comprises atmospheric neutrinos, atmospheric muons (remaining after event selection cuts), and diffuse astrophysical neutrinos. The flux is uniform in time and R.A.
2. *Signal hypothesis* $H_1(\theta_1)$. There is a signal component in addition to the atmospheric background and the average diffuse astrophysical neutrino emission. The signal neutrinos cluster around their source (subscript S) at R. A., decl. $\mathbf{x}_S = (\alpha_S, \delta_S)$. The energy spectrum of the emitted flux is an unbroken power law: $\frac{d\phi}{dE_\nu} \propto E_\nu^{-\gamma}$. In the specific case of a transient source hypothesis (see Section 2.2), the neutrino emission has a Gaussian time profile with mean μ_T and width σ_T .

We remove the high-energy alert+ events that triggered this analysis from the data set. Hence, we look for additional neutrino emission from the direction of the high-energy alert+ events. We then maximize the likelihood, \mathcal{L} , and compute the likelihood ratio,

$$\lambda(\mathbf{x}) = \frac{\sup \mathcal{L}(H_0)}{\sup \mathcal{L}(H_1)}. \quad (1)$$

The likelihood maximization varies the expectation value of the number of detected signal neutrinos, n_S , and the emitted energy spectral index, γ . We allow values for γ between 1.5 and 4. For the background hypothesis, n_S is fixed to 0.

The likelihood is the probability density of observing the data given a specific hypothesis. The probability density of observing an event, i , is a sum of its probability to be signal, S_i ,

or background, B_i : $\frac{n_S}{N}S_i + \left(1 - \frac{n_S}{N}\right)B_i$, where N is the total number of detected events (signal and background combined).

We define the test statistic (TS) as

$$\begin{aligned} \text{TS} &= -2 \ln \lambda = -2 \ln \left[\frac{\mathcal{L}(\hat{\theta}_0 | \mathbf{x}_S)}{\mathcal{L}(\hat{\theta}_1 | \mathbf{x}_S)} \right] = 2 \ln \left[\frac{\mathcal{L}(n_S = \hat{n}_S)}{\mathcal{L}(n_S = 0)} \right] \\ &= 2 \sum_i \ln \left[\frac{\hat{n}_S}{N} \left(\frac{S_i}{B_i} - 1 \right) + 1 \right] \end{aligned} \quad (2)$$

for a signal hypothesis with the best-fit value of \hat{n}_S neutrinos (where the “ $\hat{\cdot}$ ” denotes the best fit of a parameter) as the mean number of neutrinos we expect to detect from the neutrino source.

The investigated source candidates have directional uncertainties (see Figure 1). However, we assume that potential sources are smaller than the best resolution of $0^\circ.2$ in our data (TXS 0506+056 has an angular size of $\sim 2''6$). Hence, we fit the best point-source position within a reconstructed 90% uncertainty region by dividing the region into a grid with steps of $0^\circ.2$ in R.A. and decl., the best angular uncertainty for events used in this study. The likelihood is optimized at each grid point. The grid point yielding the best result (i.e., the highest TS value) is subsequently considered the point-source position.

This procedure is run on different realizations of background data $\sim 10^4$ times. The background data are all 11 yr of muon tracks with randomly assigned right ascensions. In the final step, we calculate the TS value, TS_{data} , for the true data and compare this with the simulated background TS distribution. The local p -value is the probability of getting this TS_{data} (or a larger value) from a random background realization. This procedure is repeated for all remaining regions in the sky, yielding 122 local p -values. From these 122 values, we take the most significant local p -value, p_0 , to identify the most significant source.

As a next step, we correct the significance for having tested 122 regions in the sky. Considering only background realizations, we take the most significant p -value out of 122 positions for each realization and generate a distribution of best local p -values, $p_{0,\text{BG}}$. The final global p -value of our analysis is the probability of $p_{0,\text{BG}}$ being at least as significant as the p -value we got from our real data, p_0 . Since we are investigating only a limited number of points (122), weaker neutrino emissions have a higher significance in this analysis than in an all-sky scan, for example, in Abbasi et al. (2022a).

When testing the method with Monte Carlo simulations, the best-fit number of signal neutrinos, \hat{n}_S , and source spectral index, $\hat{\gamma}$, show a bias compared to the true simulated source properties. For sources with simulated hard spectral indices (i.e., $\gamma = 2$), there is a tendency to fit slightly softer spectra and

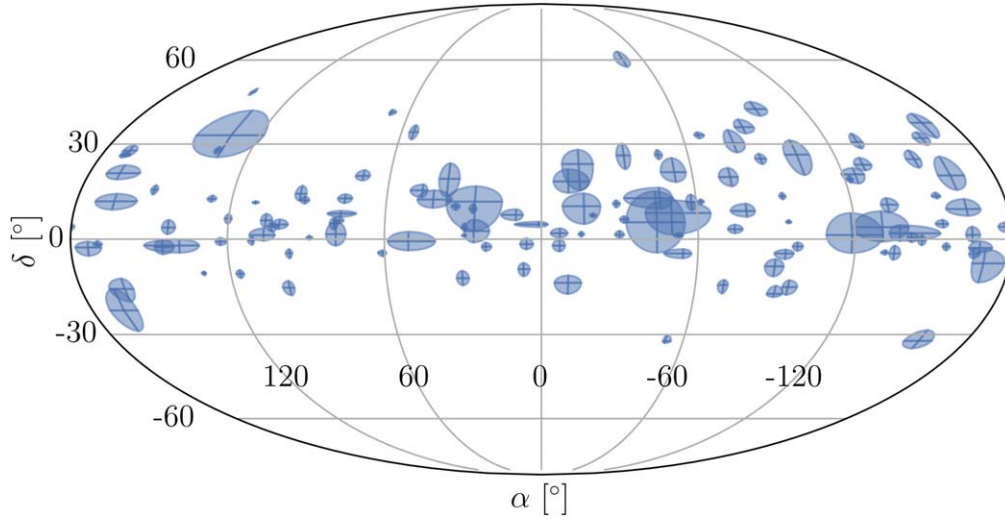


Figure 1. Sky map in R.A. and decl. (epoch = J2000) with the arrival directions of events fulfilling the IceCube alert criteria (with the highest probability of being of astrophysical origin) we investigate in this work. The events were detected between 2009 August and the end of 2021. The shaded regions represent the 90% uncertainty region of the reconstruction.

a slightly larger number of signal neutrinos. For simulated sources following softer spectral indices (i.e., $\gamma = 3$), the tendency is reversed to fitting slightly harder spectral indices and smaller numbers of signal neutrinos. Appendix A presents a more in-depth discussion of this bias. Correcting the bias is not straightforward, and we have decided not to include an at best incomplete correction. Hence, the best-fit fluxes are only indicative. This bias does not affect the flux limits since they are based on simulated fluxes where the true source strength is known.

2.1. Time-integrated Search for Continuous Sources

We define the signal and background probability density functions (pdfs) S_i and B_i in spatial and energy parts (see, e.g., Braun et al. 2008; Abbasi et al. 2011). The spatial part depends on the source position \mathbf{x}_S and the reconstructed event properties: the reconstructed origin \mathbf{x}_i and the angular uncertainty of the reconstructed origin σ_i . The energy part depends on the reconstructed muon energy, E_i ; the reconstructed origin decl., δ_i ; and the source energy spectral index, γ . The signal pdf for a steady source is hence

$$\begin{aligned} S_i(\mathbf{x}_i, E_i | \sigma_i, \mathbf{x}_S, \gamma) &= S_{\text{spatial}}(\mathbf{x}_i | \sigma_i, \mathbf{x}_S) \cdot S_{\text{energy}}(E_i | \delta_i, \gamma) \\ &= \frac{1}{2\pi\sigma_i^2} \exp\left(-\frac{|\mathbf{x}_i - \mathbf{x}_S|^2}{2\sigma_i^2}\right) \cdot S_{\text{energy}}(E_i | \delta_i, \gamma). \end{aligned} \quad (3)$$

The energy pdf, S_{energy} , is the probability of detecting a neutrino with reconstructed energy, E_i , at decl., δ_i , assuming the source emits neutrinos with a spectrum of $E^{-\gamma}$. The background pdfs, B_i , are defined similarly:

$$\begin{aligned} B_i(\mathbf{x}_i, E_i) &= B_{\text{spatial}}(\mathbf{x}_i) \cdot B_{\text{energy}}(E_i | \delta_i) \\ &= \frac{1}{2\pi} \cdot P(\delta_i) \cdot B_{\text{energy}}(E_i | \delta_i). \end{aligned} \quad (4)$$

The spatial term depends only on the event decl., δ_i . We assume uniformity in R.A. for the background data due to IceCube's unique position at the South Pole. B_{energy} is derived directly from experimental data.

Searching for neutrino counterparts of the alert+ events, we want to be sensitive to a single strong emission from one source (or a few sources) and, additionally, to faint emissions from a larger number of sources. Hence, our search for continuous sources consists of two parts. The first part searches for single strong neutrino emitters. The second part investigates the overall neutrino emission from all 122 positions of interest. In the latter case, we combine the neutrino emission and define a new TS value, $\text{TS}_{\text{stacked}}$, by summing the TS values of all alert+ positions, k ,

$$\text{TS}_{\text{stacked}} = \sum_k \text{TS}_k. \quad (5)$$

We take the TS_k from the individual search; hence, we do not correct for overlapping uncertainty regions of alert+ events.

2.2. Transient Sources

For transient sources, we multiply a temporal pdf with the previously defined spatial and energy pdfs in Equations (3) and (4) (Braun et al. 2010). We assume a Gaussian-shaped time profile centered around μ_T with width σ_T for the signal part. The temporal signal pdf becomes

$$S_T(t_i | \mu_T, \sigma_T) = \frac{1}{\sigma_T \sqrt{2\pi}} \exp\left(-\frac{(t_i - \mu_T)^2}{2\sigma_T^2}\right), \quad (6)$$

with t_i as the time the event was detected. The background expectation is a constant rate over the whole data-taking time, t_{data} :

$$B_T = \frac{1}{t_{\text{data}}}. \quad (7)$$

The search for time-dependent sources adds another optimization step for the best flaring time. This introduces a bias toward shorter flares since the number of possible shorter flares is larger than the number of possible longer flares. We correct for this effect by multiplying the TS by a marginalization factor, $\frac{\sqrt{2\pi}\sigma_T}{300 \text{ days}}$ (Braun et al. 2010). Here, 300 days is the maximal flaring time. Longer timescales would result in

worse sensitivity than the time-integrated search. We assume a minimal σ_T of 5 days to ensure the background uniformity in R.A.

Conventional methods to find neutrino flares as in Aartsen et al. (2015, 2018b) and Abbasi et al. (2021c, 2021d) apply a brute-force scan of all possible time intervals between events where the ratio of Equation (3) over Equation (4) exceeds a certain threshold. This is computationally expensive. The computational cost can be reduced by increasing the required threshold and hence reducing the possible number of intervals scanned. We want to include as few biases as possible, and if following conventional approaches, we would apply the same threshold as in Aartsen et al. (2018b), where the ratio had to be ≥ 1 . However, Aartsen et al. (2018b) performs this search only on one position in the sky. In our case, this would mean scanning the uncertainty region of 122 alert+ events in steps of 0.2° and, at each step, evaluating every possible time window between 5 and 300 days in 11 yr for neutrino emission. This proved to be computationally unfeasible. To overcome this problem, we investigated new approaches (Karl et al. 2021, 2023; Karl 2022) that do not rely on thresholds, such as a different TS to evaluate if an emission is time-dependent (Eller & Shtembari 2023) or finding an analytical description of the TS such that we would not need to simulate a large number of background and signal models.

Here, we have applied an unsupervised-learning algorithm looking for clustering in data: expectation maximization (Dempster et al. 1977). This is the first time we apply expectation maximization to IceCube data and use it to fit the best time of transient neutrino emission.

The procedure is as follows (Karl & Eller 2023). For a source position to be tested (grid point), we assume a two-component mixture model for the temporal distribution of our data (a neutrino flare in the form of a Gaussian signal and uniform background). As a starting flare, we choose a single very broad flare, extending beyond the whole data-taking period. For each event, we compute the probability of it belonging to the neutrino flare (the membership probability). These probabilities are then used to improve the flare parameters iteratively. In the calculation of the membership probability for event i , we include the pdf values for the spatial and energy signal and background pdfs (as in Equations (3) and (4)) as event weights. The membership probability is

$$\begin{aligned} P_{i,\text{flare}} &= \frac{\frac{n_{\text{flare}}}{N} S_i S_T(t_i | \mu_T, \sigma_T)}{\frac{n_{\text{flare}}}{N} S_i S_T(t_i | \mu_T, \sigma_T) + (1 - \frac{n_{\text{flare}}}{N}) B_i B_T} \\ &= \frac{n_{\text{flare}} \frac{S_i}{B_i} S_T(t_i | \mu_T, \sigma_T)}{n_{\text{flare}} \frac{S_i}{B_i} S_T(t_i | \mu_T, \sigma_T) + \frac{N - n_{\text{flare}}}{t_{\text{data}}}}, \end{aligned} \quad (8)$$

and at each iteration, the mean time, μ_T , and the width, σ_T , are recalculated using

$$\mu_T = \frac{\sum_i P_{i,\text{flare}} t_i}{\sum_i P_{i,\text{flare}}} \quad (9)$$

and

$$\sigma_T = \frac{\sum_i P_{i,\text{flare}} (t_i - \mu_T)^2}{\sum_i P_{i,\text{flare}}}. \quad (10)$$

The quantity n_{flare} scales the Gaussian temporal pdf according to the expected number of signal events. However, n_{flare} is only

used to determine μ_T and σ_T ; n_S is fitted independently once we determine the time pdf of the neutrino flare. We stop the iterations when there is no change in the likelihood in the past 20 iterations or once 500 iterations have been performed.

The signal weight, S_i/B_i , depends on the assumed source spectral index, γ . We want to avoid favoring a specific index; hence, we run expectation maximization for different fixed spectral indices, γ_{EM} , between 1.5 and 4 in steps of 0.2 (Karl & Eller 2023). We get an optimized time pdf for each γ_{EM} . We then optimize the TS as in Equation (2) with the signal and background pdfs, including the temporal pdfs for each γ_{EM} . In this step, we fit n_S and γ while keeping the temporal pdf with $\hat{\mu}_T(\gamma_{\text{EM}})$ and $\hat{\sigma}_T(\gamma_{\text{EM}})$ fixed. The flare yielding the highest TS value is then the best-fit flare for this grid point. For each alert +, we repeat this procedure at every grid point in the uncertainty region. The point with the most significant result is then the preferred source location. For the background TS distribution, we shuffled the event times and calculated the new R.A. values based on the event azimuths and the shuffled times.

3. Results

3.1. Continuous Sources

The search for the strongest single continuous source yields a global p -value of 0.98 and is compatible with the background hypothesis. We determine an upper flux limit by simulating neutrino emission with an E^{-2} spectrum. The upper flux limit is the flux for which 90% of the corresponding TS distribution lies above the TS value of the strongest single continuous source. We get an upper flux limit (for muon neutrinos and antineutrinos) at a 90% confidence level for the most significant position of $\Phi_{90\%,100\text{ TeV}}^{\nu_\mu + \bar{\nu}_\mu, \text{single}} = 6.9 \times 10^{-17} (\text{TeV cm}^2 \text{s})^{-1}$. In general, the energy-dependent flux, $\Phi(E)$, of this flux limit is $\Phi(E) = \Phi_{90\%,100\text{ TeV}}^{\nu_\mu + \bar{\nu}_\mu, \text{single}} \times \left(\frac{E}{100\text{ TeV}}\right)^{-2}$. The acceptance for the simulated flux has a limited range in energy. We define the energy range for the flux limit as the central 90% quantile of detected simulated events. In this case, we limit the flux from 0.9 to 483 TeV. Table 4 lists the results for all 122 investigated regions.

For the combined emission of all sources, we get a p -value of 8%, which is also compatible with the background hypothesis. We determine the 90% confidence level upper flux limit, $\Phi_{90\%,100\text{ TeV}}^{\nu_\mu + \bar{\nu}_\mu, \text{stacked}}$, by simulating an increasing number of sources emitting a weak flux, ϕ_1 , corresponding to one neutrino coming from a source at the celestial equator—IceCube’s most sensitive region for detecting neutrinos at the highest energies—in 11 yr ($\phi_1 = 4.502 \times 10^{-18} (\text{TeV cm}^2 \text{s})^{-1}$). We repeat the simulation $\sim 10^4$ times for each combined flux and create a $\text{TS}_{\text{stacked}}$ distribution. Based on this distribution, we determine the combined flux that is strong enough to yield a higher TS value than our result with 90% probability.

The upper limit of emission additional to the alert+ events is $\Phi_{90\%,100\text{ TeV}}^{\nu_\mu + \bar{\nu}_\mu, \text{stacked}} = 4.2 \times 10^{-16} (\text{TeV cm}^2 \text{s})^{-1}$ for a spectral index of $\gamma = 2$ and within the energy range from 4.2 TeV to 3.6 PeV. For comparison, the diffuse astrophysical neutrino flux is $\Phi_{\text{diffuse},100\text{ TeV}} = 1.44 \times 10^{-15} (\text{TeV cm}^2 \text{s sr})^{-1}$ in the range of 15 TeV to 5 PeV (Abbasi et al. 2022b) with a spectral index of $\gamma = 2.37$. Integrating over the energy range where both the diffuse flux and $\Phi_{90\%,100\text{ TeV}}^{\nu_\mu + \bar{\nu}_\mu, \text{stacked}}$ overlap, $\Phi_{90\%,100\text{ TeV}}^{\nu_\mu + \bar{\nu}_\mu, \text{stacked}}$ corresponds to 1.6% of the astrophysical diffuse flux. To constrain the maximal possible emission from the alert+ regions, including

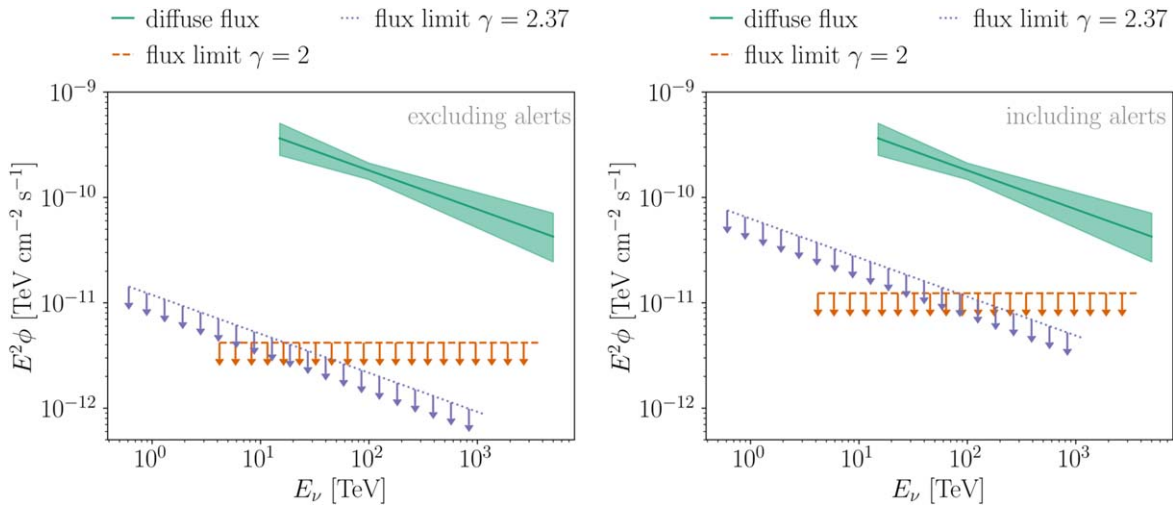


Figure 2. 90% confidence level upper flux limits for all source candidates combined (dashed orange line) valid in the energy range of 4.2 TeV to 3.6 PeV and a neutrino emission following E^{-2} . The green line is the diffuse astrophysical neutrino flux ($\Phi_{\text{diffuse}, 100 \text{ TeV}} = 1.44 \times 10^{-15} \cdot 4\pi (\text{TeV cm}^2 \text{s})^{-1}$) in the range of 15 TeV to 5 PeV (Abbasi et al. 2022b). The dotted purple line shows the 90% confidence level upper flux limit combining all sources for the spectral index of the diffuse flux ($\gamma = 2.37$) between 0.6 TeV and 1 PeV. Left: the upper flux limit, excluding the alert+ events in the analyzed data, is 1.6% ($\gamma = 2$) of the astrophysical diffuse flux in the overlapping energy range and 1.5% when assuming the same spectral index ($\gamma = 2.37$) as for the astrophysical diffuse flux. Right: the upper flux limit, including the alert+ events in the data, is 4.5% of the astrophysical diffuse flux in the overlapping energy range for $\gamma = 2$ and 8% of the diffuse flux when assuming the same spectral index ($\gamma = 2.37$) as for the astrophysical diffuse flux.

the highest-energy events, we include the alert+ events just for the following limit. Thus, considering the total emission of all 122 regions, including alert+ events, we get an upper flux limit of $\Phi_{90\%, 100 \text{ TeV}}^{\nu_{\mu} + \nu_{\tau}, \text{with alerts}} = 1.2 \times 10^{-15} (\text{TeV cm}^2 \text{s})^{-1}$ for the energy range from 4.2 TeV to 3.6 PeV, which corresponds to 4.5% of the diffuse astrophysical neutrino flux where both fluxes overlap in their energy range (see Figure 2). We repeat the upper flux limit calculation with the same spectral index as for the astrophysical diffuse flux and get a limit of $2.1 \times 10^{-16} (\text{TeV cm}^2 \text{s})^{-1}$ (1.5% of the astrophysical diffuse flux) excluding alert+ events and $1.1 \times 10^{-15} (\text{TeV cm}^2 \text{s})^{-1}$ including alert+ events (8% of the astrophysical diffuse flux) at 100 TeV. For $\gamma = 2.37$, the energies of the simulated detected events range from 0.6 TeV to 1 PeV. This energy range differs from the previous range for $\gamma = 2$. The energy distribution of the signal events depends on the simulated energy spectral index. There are more neutrinos in lower energies if the simulated energy spectrum is softer compared to a harder emission.

The lack of lower-energy neutrino emission (compared to IceCube alert+ events) could be caused by various scenarios. It is, for example, possible that some sources flare in neutrinos, emitting mainly high-energy neutrinos. Another possibility might be a hard neutrino emission, i.e., $\gamma \leq 1$ (for example, models proposed in Waxman & Bahcall 1999; Padovani et al. 2022). The atmospheric background would dominate the lower-energy neutrino emission. The higher-energy neutrino emission would be detected as single high-energy events, given IceCube’s effective area (Aartsen et al. 2020; Abbasi et al. 2021b). This matches our observation. However, there are many different scenarios that agree with this work. In these cases, different source populations or states produce different neutrino spectra compared to one continuous power law. Another possible scenario including a source population emitting single power laws is described in Abbasi et al. (2023b). Our result agrees with the high-density scenario presented in Section 6 of Abbasi et al. (2023b). There, a high-density source population with low individual fluxes (with an

$E^{-2.5}$ energy spectrum) is the origin of alert events. Due to the sheer number of sources, we would be able to detect flux fluctuations in high energies as alert events without a detectable lower-energy component. In lower energies, the flux would be too low to be detected, and it would require a simultaneous fluctuation in both lower and higher energies such that both components could be detected from the same object.

3.2. Transient Sources

In our search for transient sources, we look for the most significant transient neutrino emission. Out of all 122 investigated alert+ origins, the most significant transient emission is the neutrino flare with the seed alert IceCube-170922A, which is associated with the blazar TXS 0506+056. Our search yields a local p -value of 0.14% (or a significance of 3σ). The main differences between the search in Aartsen et al. (2018b) and this work are as follows.

1. We have no external trigger in this work, whereas Aartsen et al. (2018b) were triggered by the observation of a flaring blazar.
2. We use 11 yr of recalibrated IceCube muon data, improving directional and energy reconstruction. For a discussion of how the contributing events are affected, see Appendix B.
3. We include a fit for the best source position and use expectation maximization to identify the time of the neutrino flare.

The corresponding flare is centered around a mean flare time $\hat{t}_T = 57001_{-26}^{+38}$ MJD and has a width of $\hat{\sigma}_T = 64_{-10}^{+35}$ days. These properties agree with Aartsen et al. (2018b), as shown in Figure 3. When correcting for the look-elsewhere effect, the global p -value is $p_{\text{global}} = 0.156$, which is not significant. Such a trial correction does not apply for the search reported in Aartsen et al. (2018b). Table 5 lists all results for the investigated regions.

The best-fit parameter can yield insight into the source emission. However, as mentioned in Section 2 and

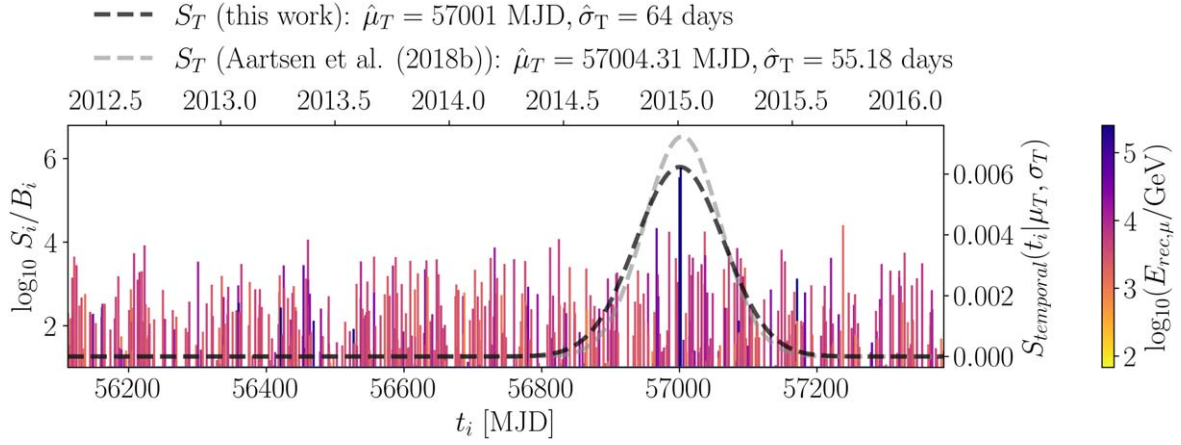


Figure 3. Logarithm of the signal-over-background ratio, $\log_{10} S_i/B_i$, distribution of individual events, i , vs. their detection time, t_i , between 2012 and 2016. The $\log_{10} S_i/B_i$ values are for the best-fit position (close to TXS 0506+056) and the best-fit spectral index. The color indicates the reconstructed muon energy, $E_{\text{rec},\mu}$, increasing from light to dark. The black dashed line shows this work's best-fit time pdf S_T (with the y-axis on the right). It agrees with the gray dashed pdf of Aartsen et al. (2018b).

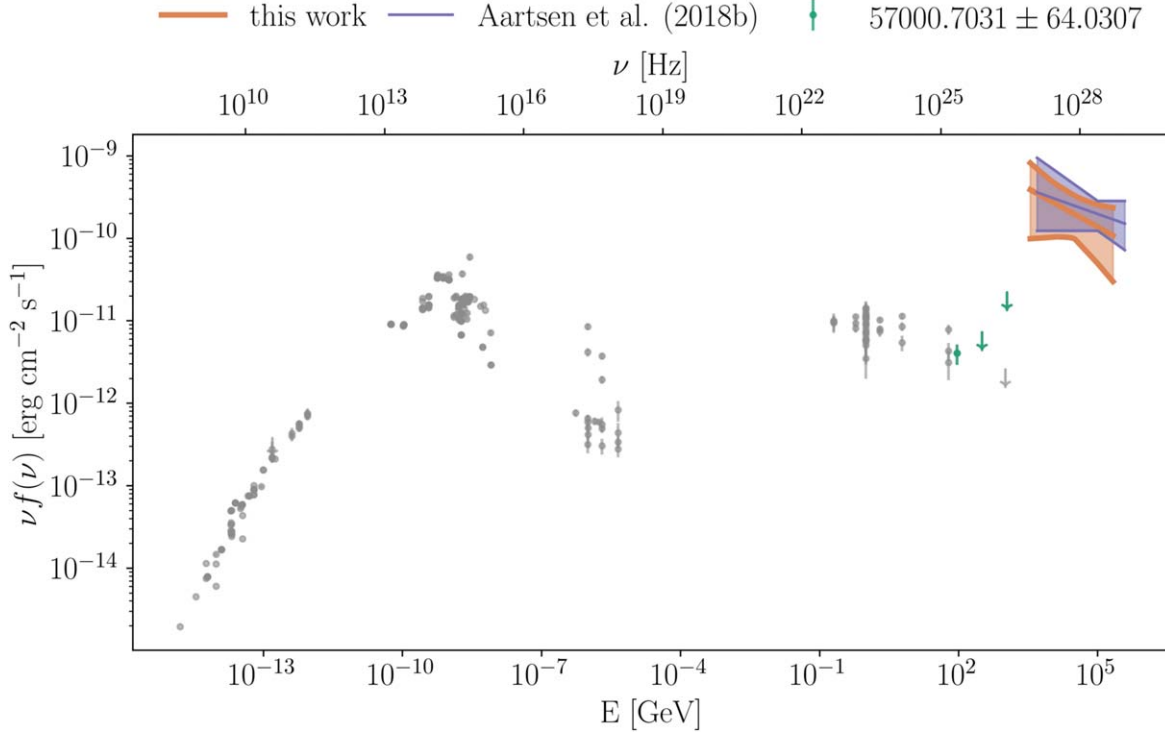


Figure 4. Spectral energy distribution of TXS 0506+056 in photons (gray dots) and neutrinos during the time of the neutrino flare (bands). The green dots (arrows) show gamma-ray emission (upper limits) during the time window of the neutrino flare detected by Fermi-LAT (Ackermann et al. 2012). This work's all-flavor neutrino flux during the flare (orange band; $3 \times \Phi_{100 \text{ TeV}}^{\nu_\mu + \bar{\nu}_\mu}$) agrees with the all-flavor flux given in White & Becker (1992); Wright et al. (1994, 2010); Gregory et al. (1996); Condon et al. (1998); Voges et al. (1999); Data for the photon SED are from Myers et al. (2003); Healey et al. (2007); Jackson et al. (2007); Nieppola et al. (2007); Abdo et al. (2010); Planck Collaboration et al. (2011, 2014, 2016); Bianchi et al. (2011); Bartoli et al. (2013); D'Elia et al. (2013); Evans et al. (2014); Boller et al. (2016); Nolan et al. (2012); Acero et al. (2015); Aartsen et al. (2018b; dark purple band). Giommi et al. (2018).

Appendix A, the best-fit results and the resulting flux estimations are biased. The best-fit result of the number of neutrinos in the neutrino flare is $\hat{n}_S = 12_{-7}^{+9}$ with a spectral index of $\hat{\gamma} = 2.3 \pm 0.4$. This corresponds to an average flux of $\Phi_{100 \text{ TeV}}^{\nu_\mu + \bar{\nu}_\mu} = 1.1_{-0.8}^{+0.9} \times 10^{-15} \text{ (TeV cm}^2 \text{ s)}^{-1}$ in the energy range of 3.5–213 TeV during the period of the neutrino flare. The corresponding single-flavor neutrino and antineutrino fluence, the flux integrated over the flaring period ($\hat{\mu}_T - 2\hat{\sigma}_T$ to $\hat{\mu}_T + 2\hat{\sigma}_T$), is $J_{100 \text{ TeV}}^{\nu_\mu + \bar{\nu}_\mu} = 1.2_{-0.8}^{+1.0} \times 10^{-8} \text{ (TeV cm}^2 \text{)}^{-1}$. This flux estimation also agrees with Aartsen et al. (2018b), as shown by the all-flavor neutrino flux (three times $\Phi_{100 \text{ TeV}}^{\nu_\mu + \bar{\nu}_\mu}$) in

Figure 4. In Appendix B, we compare the events contributing to the neutrino flare in this analysis and previous works and explain why the errors differ.

For transient emission, the lack of additional lower-energy neutrino emission (besides the reported local evidence associated with TXS 0506+056) can imply various scenarios. One is that neutrino flares occur rarely or might not necessarily be connected to the production sites of high-energy neutrinos. Similar to Section 3.1, it could also indicate that these neutrino sources emit a very hard energy spectrum, for example, with $\gamma \leq 1$.

4. Conclusion

Our study focused on the origin of IceCube’s highest-energy events, or alert+ events, to identify potential sources of additional neutrino emission. To achieve this, we systematically scanned the 90% uncertainty contours of reconstructed alert+ events with a resolution of 0.2° to determine the most significant source position. We assumed that the emission followed a power-law distribution, $\propto E^{-\gamma}$, with γ ranging from 1.5 to 4.

Our analysis found no evidence for continuous emission from a single source, as the data were consistent with the background assumption. Therefore, we placed a constraint on the overall combined flux from all positions, which was found to be 1.6% of the diffuse astrophysical neutrino flux observed by IceCube (for $\gamma=2$). If we included the alert+ events in the analysis, we could constrain all expected emissions from their respective directions to no more than 4.5% of the diffuse astrophysical neutrino flux (for $\gamma=2$). For a source spectral index similar to the diffuse astrophysical neutrino flux ($\gamma=2.37$), we constrain the overall combined flux to be less than 1.5% (excluding the alert+ events) and less than 8% (including the alert+ events) of the diffuse astrophysical neutrino flux. This indicates that different source populations or states produce different neutrino spectra compared to one continuous power law.

Our investigation confirmed the neutrino flare associated with the blazar TXS 0506+056 as the most significant transient emission from all investigated positions, with a local significance of about 3σ . When we corrected for the look-elsewhere effect in this analysis, the global significance was 15.6%, consistent with the background expectation. The parameters of the neutrino flare in this study using recalibrated data agreed with previously published results. We identified a Gaussian time window with a center at 57001_{-26}^{+38} MJD and a width of 64_{-10}^{+35} days as the best fit and estimated that 12_{-6}^{+9} neutrinos were detected during the flare with a best-fit spectral index of $\hat{\gamma} = 2.3 \pm 0.4$. This corresponds to a single-flavor neutrino fluence of $J_{100\text{ TeV}}^{\nu_\mu+\nu_\tau} = 1.2_{-0.8}^{+1.0} \times 10^{-8}$ (TeV cm²)⁻¹ and an average flux of $\Phi_{100\text{ TeV}}^{\nu_\mu+\nu_\tau} = 1.1_{-0.8}^{+0.9} \times 10^{-15}$ (TeV cm² s)⁻¹ during the $2\sigma_T$ time window. However, we find no other alert+ event with a similar local significance. TXS 0506+056 remains the only source candidate where we find the connection of a high-energy alert and a lower-energetic neutrino emission.

For neither continuous nor transient emission did we find evidence of a lower-energy neutrino component. This can be explained in various scenarios. One is a hard neutrino spectrum with $\gamma \leq 1$. In such a scenario, atmospheric background noise would dominate the lower-energy range, while the higher-energy range would yield single high-energy events. It could also be caused by a high-density source population as investigated in Abbasi et al. (2023b), where high-energy events are the result of fluctuations from a large population of sources with individually weak fluxes. In this case, the lower-energy flux would still be too low to be detected. Our finding also suggests that neutrino flares may be rare or produced at different sites than IceCube alert+ events or that there are sources mainly emitting high-energy neutrinos.

Acknowledgments

The IceCube Collaboration acknowledges significant contributions to this manuscript from Martina Karl. The authors gratefully acknowledge the support from the following agencies and institutions: USA—U.S. National Science Foundation Office of

Polar Programs, U.S. National Science Foundation Physics Division, U.S. National Science Foundation EPSCoR, U.S. National Science Foundation Office of Advanced Cyberinfrastructure, Wisconsin Alumni Research Foundation, Center for High Throughput Computing (CHTC) at the University of Wisconsin–Madison, Open Science Grid (OSG), Partnership to Advance Throughput Computing (PATH), Advanced Cyberinfrastructure Coordination Ecosystem: Services & Support (ACCESS), Frontera computing project at the Texas Advanced Computing Center, U.S. Department of Energy National Energy Research Scientific Computing Center, particle astrophysics research computing center at the University of Maryland, Institute for Cyber-Enabled Research at Michigan State University, astroparticle physics computational facility at Marquette University, NVIDIA Corporation, and Google Cloud Platform; Belgium—Funds for Scientific Research (FRS-FNRS and FWO), FWO Odysseus and Big Science programs, and Belgian Federal Science Policy Office (Belspo); Germany—Bundesministerium für Bildung und Forschung (BMBF), Deutsche Forschungsgemeinschaft (DFG), Helmholtz Alliance for Astroparticle Physics (HAP), Initiative and Networking Fund of the Helmholtz Association, Deutsches Elektronen Synchrotron (DESY), and High Performance Computing cluster of the RWTH Aachen; Sweden—Swedish Research Council, Swedish Polar Research Secretariat, Swedish National Infrastructure for Computing (SNIC), and Knut and Alice Wallenberg Foundation; European Union—EGI Advanced Computing for Research; Australia—Australian Research Council; Canada—Natural Sciences and Engineering Research Council of Canada, Calcul Québec, Compute Ontario, Canada Foundation for Innovation, WestGrid, and Digital Research Alliance of Canada; Denmark—Villum Fonden, Carlsberg Foundation, and European Commission; New Zealand—Marsden Fund; Japan—Japan Society for Promotion of Science (JSPS) and Institute for Global Prominent Research (IGPR) of Chiba University; Korea—National Research Foundation of Korea (NRF); Switzerland—Swiss National Science Foundation (SNSF).

Appendix A Parameter Recovery

When testing the method, as described in Section 2, with Monte Carlo simulations (Karl 2022), the best-fit number of signal neutrinos, n_S , and source spectral index, γ , show a bias compared to the true simulated source properties. For sources with simulated hard spectral indices (i.e., $\gamma=2$), there is a tendency to fit slightly softer spectra and a slightly larger number of signal neutrinos. For example, simulating an average of 10 neutrinos with $\gamma=2$ results in a mean best fit of $\hat{n}_S = 16$ and $\hat{\gamma} = 2.25$. For simulated sources following softer spectral indices (i.e., $\gamma=3$), the tendency is reversed to fitting slightly harder spectral indices and smaller numbers of signal neutrinos.

Several aspects influence this bias. One is a simplified spatial distribution in the form of a Rayleigh distribution (see Equation (3)). This is corrected using a kernel density estimation (KDE) approach, for example, in Abbasi et al. (2022a). However, the KDE approach is, so far, only feasible in the northern sky. Since we also search for neutrino sources from the southern sky, we chose the simplified method. Another aspect is that weak sources emitting only a few neutrinos are not always found during the position scan, since background fluctuations can dominate these weak sources. For example, for a continuous emission over 11 yr, the mean distance between the best-fit source position and the actual

simulated source is smaller than 0.3 for a flux resulting in five signal neutrinos on average. This also means that the best-fit n_S will be larger than 0 in many cases with no neutrino source, since the algorithm will find the position with the largest background fluctuation. Hence, correcting this bias is not straightforward, and this analysis is mainly sensitive to strong neutrino sources.

For transient sources, the bias is smaller. In the same example as above, 10 neutrinos with $\gamma=2$ emitted over a period of $\sigma_T \approx 55$ days are a much stronger signal compared to 10 neutrinos over 11 yr. Hence in this specific case, the mean best-fit $\hat{n}_S = 12$ and the best-fit $\hat{\gamma} = 2.1$. However, we still face the case that background fluctuations can dominate weak neutrino emission (in the case of $\sigma_T \approx 55$ days, anything below five neutrinos is difficult), which makes correcting this bias challenging. We have decided not to include an at best incomplete correction in this work. For now, measurements of point-source fluxes are only possible with the KDE approach.

Appendix B Transient Sources Analysis

Figure 5 shows the p -value map of the scanned region around IceCube-170922A on the left. The most significant

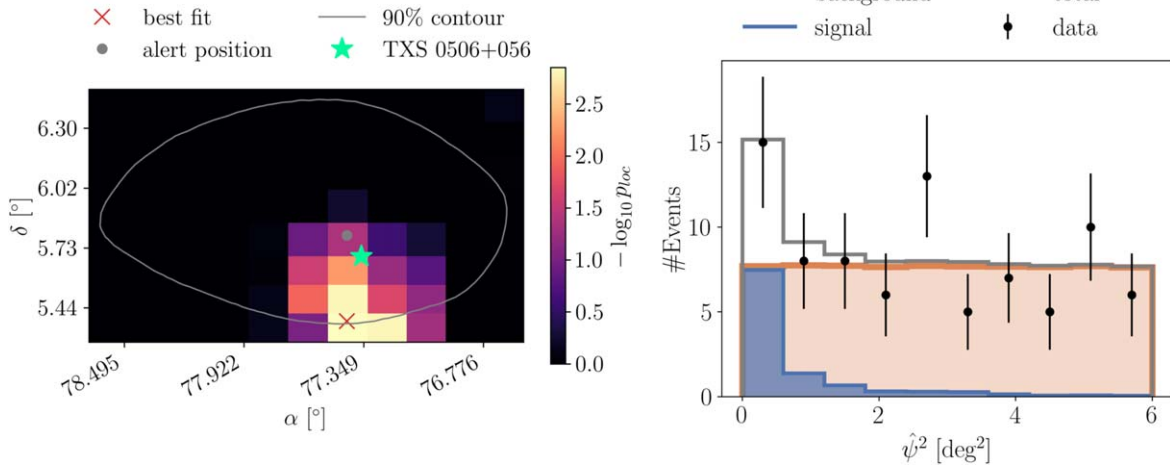


Figure 5. Left: p -value map of the alert region of IceCube-170922A. The gray dot indicates the reconstructed direction of IceCube-170922A, and the gray contour shows the 90% uncertainties of the reconstruction. The red cross marks the best-fit position of the position scan (0.6 from the reconstructed alert position). The star shows the location of TXS 0506+056. All black bins have p -values close to 1. Right: number of events at binned squared angular distances, $\hat{\psi}^2$, between TXS 0506+056 and the reconstructed event directions during the neutrino flare ($57001 \text{ MJD} \pm 2 \times 64$ days). Scrambled data in R.A. provide the background (blue), and Monte Carlo simulations for the best-fit flux ($n_S = 12$ and $\gamma = 2.31$) yield the signal (orange). The gray line combines the background with the signal and matches the data points (black). The data are shown with 68% uncertainties.

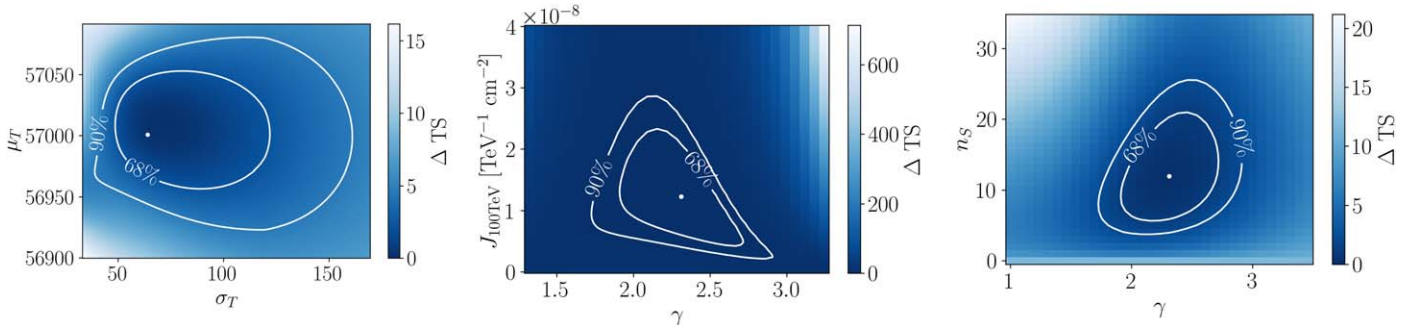


Figure 6. Change of the TS value for the different likelihood parameters. Left: profiled change for different μ_T and σ_T . n_S and γ are optimized at each step. The 68% uncertainties are $\hat{\mu}_T = 57001_{-26}^{+38}$ MJD and $\hat{\sigma}_T = 64_{-10}^{+35}$ days. Center: change when varying the signal fluence $J_{100 \text{ TeV}}^{\nu_\mu + \bar{\nu}_\mu}(n_S, \gamma)$. The 68% uncertainties on the fluence are $J_{100 \text{ TeV}}^{\nu_\mu + \bar{\nu}_\mu} = 1.2_{-0.8}^{+1.0} \times 10^{-8} (\text{TeV cm}^2)^{-1}$. Right: variation when changing n_S and γ . The 68% uncertainties are $\hat{n}_S = 12_{-7}^{+9}$ and $\hat{\gamma} = 2.3 \pm 0.4$.

position is within 0.5 from TXS 0506+056. The right panel of Figure 5 shows a histogram of the angular distance of events from TXS 0506+056. There is a clustering of events around the source position. The signal events for this plot are simulated according to the best-fit result of the likelihood ratio test ($\hat{n}_S = 12$, $\hat{\gamma} = 2.3$). The background distribution is scrambled data in R.A. The signal on top of the background flux matches the observed data.

To determine the uncertainties of the best-fit values, we run a likelihood scan over the parameter space and use Wilk's theorem (Wilks 1938) to determine the 68% and 90% contours (see Figure 6). These contours are relevant for the two-dimensional uncertainties of the flux as in Figure 4. For the time, we determine the profiled change of the TS for different μ_T and σ_T . The best n_S and γ are fitted for each value. The 68% uncertainties determined by a profiled change of the TS are $\hat{\mu}_T = 57001_{-26}^{+38}$ MJD and $\hat{\sigma}_T = 64_{-10}^{+35}$ days. The one-dimensional errors for fluence, number of signal neutrinos n_S , and spectral index γ are determined with the profiled change of the TS where the mean flaring time and the flare width are kept fixed to the best-fit values. For the signal fluence, the 68% uncertainties are $J_{100 \text{ TeV}}^{\nu_\mu + \bar{\nu}_\mu} = 1.2_{-0.8}^{+1.0} \times 10^{-8} (\text{TeV cm}^2)^{-1}$, and for n_S and γ , we get $\hat{n}_S = 12_{-7}^{+9}$ and $\hat{\gamma} = 2.3 \pm 0.4$.

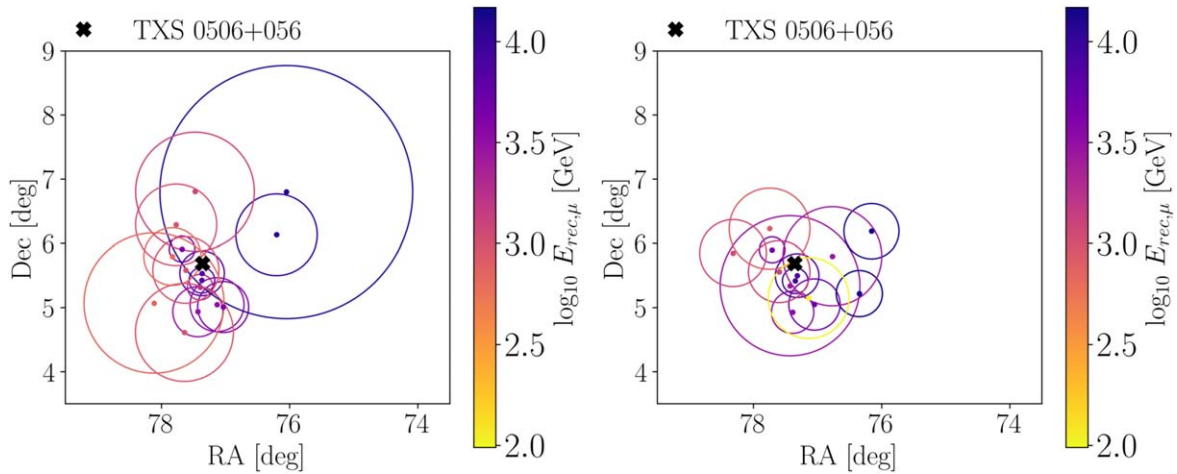


Figure 7. Position and energy (color) of the 14 events contributing the most to the TXS 0506+056 neutrino flare. The circles show the uncertainty of the directional reconstruction, σ . Left: the 14 most contributing events from the data sample used in this work (see Table 2). Right: the 14 most contributing events from the old data sample (Abbasi et al. 2021b).

Table 2
Comparison of the Top 14 Events Contributing to the Neutrino Flare of TXS 0506+056 in Different Data Sets

MJD	This Work				Abbasi et al. (2021b)				Ranking
	R.A. (deg)	Decl. (deg)	σ (deg)	$\log_{10}(E/\text{GeV})$	R.A. (deg)	Decl. (deg)	σ (deg)	$\log_{10}(E/\text{GeV})$	
56940.9084	77.36	5.42	0.20	3.81	77.35	5.42	0.20	3.97	1
57009.5301	77.36	5.53	0.34	3.85	77.32	5.50	0.34	3.91	2
56973.3971	77.03	5.01	0.39	3.61	77.05	5.05	0.40	3.71	12
57112.6530	77.39	5.32	0.20	3.23	77.43	5.34	1.09	3.46	7
57072.2088	77.13	5.04	0.42	3.50	76.35	5.22	0.36	3.43	9
56981.1313	76.20	6.13	0.63	4.03	76.16	6.19	0.43	4.13	5
57089.4395	77.67	5.91	0.20	3.62	77.71	5.90	0.20	3.69	3
56927.8601	77.43	4.93	0.39	3.46	77.39	4.93	0.33	3.53	13
56955.7917	77.61	5.58	0.51	2.99	77.60	5.56	0.48	3.09	6
57072.9895	76.05	6.80	1.97	4.09	76.35	5.22	0.36	4.17	4
56940.5215	77.82	5.79	0.44	2.80
57031.8224	77.64	4.61	0.76	2.96
56937.8189	77.77	6.29	0.63	2.98	77.75	6.23	0.63	2.91	11
56983.2476	77.47	6.80	0.92	3.09

Note. Left: Top 14 events with the strongest contribution to the neutrino flare of TXS 0506+056, sorted by significance. Right: The same events in the data sample published in Abbasi et al. (2021b). The last column states the ranking of the contribution in previous analyses. The data set used in this work has improved directional and energy reconstruction. Some events have shifted in position and have slightly different energies.

Table 2 lists the top 14 events contributing to the neutrino flare, sorted by their S_i/B_i value multiplied by S_T . We compare this with a previous data sample (Abbasi et al. 2021b; for events also included in that sample) to emphasize how the updated photomultiplier calibration affects the reconstructed direction, angular error, and energy.

The improved directional and energy reconstruction has changed the contributing events compared to previous analyses (Aartsen et al. 2018b; Abbasi et al. 2021b). Most of the significance is caused by the two most contributing events, which remain the same (see also Karl 2022). However, their position is shifted, and their energy is changed. For the remaining events, the contributing order has changed, or the events themselves differ. Figure 7 shows the position and energy of the 14 events contributing the most to the neutrino flare from the previous data set (left) and the improved data used in this work (right). The event with the largest error region

($\sigma = 1^\circ 9$) in the right panel is also included in the left panel. However, the uncertainty was underestimated in the previous data sample ($\sigma = 0^\circ 36$), and its position has shifted.

Appendix C IceCube Alert+ Events

Table 3 lists all alert+ events used in this work. The selection aims for a high signal purity and comprises alerts published in the gold alert channel (Abbasi et al. 2023a). Additionally, we include high-energy events from Abbasi et al. (2022b) that were classified to be of likely astrophysical origin by a new event classifier (Kronmueller & Glauch 2019). We excluded events within 30° of the geographic poles and events with uncertainties $\geq 100 \text{ deg}^2$. The final selection has a probability of being astrophysical of > 0.5 . We remove the respective alert+ event from IceCube data when running the analysis.

Table 3
Alert+ Events Investigated in This Work

Index	Track Name	Time (MJD)	R.A. (deg)	Decl. (deg)
1	DIF090813	55056.6983	29.51 ^{+0.40} _{-0.38}	1.23 ^{+0.18} _{-0.22}
2	DIF091106	55141.1275	298.21 ^{+0.53} _{-0.57}	11.74 ^{+0.32} _{-0.38}
3	DIF100608	55355.4872	344.93 ^{+3.39} _{-2.90}	23.58 ^{+2.31} _{-4.13}
4	DIF100623	55370.7355	141.25 ^{+0.46} _{-0.45}	47.80 ^{+0.56} _{-0.48}
5	DIF100710	55387.5362	306.96 ^{+2.70} _{-2.28}	21.00 ^{+2.25} _{-1.56}
6	DIF100925	55464.8959	266.29 ^{+0.58} _{-0.63}	13.40 ^{+0.23} _{-0.45}
7	DIF101009	55478.3806	331.09 ^{+0.56} _{-0.72}	11.10 ^{+0.48} _{-0.58}
8	DIF101028	55497.3033	88.68 ^{+0.54} _{-0.55}	0.46 ^{+0.33} _{-0.27}
9	HESE101112	55512.5516	110.56 ^{+0.80} _{-0.37}	-0.37 ^{+0.48} _{-0.65}
10	DIF101113	55513.5995	285.95 ^{+1.29} _{-1.50}	3.15 ^{+0.70} _{-0.63}
11	DIF110128	55589.5628	307.53 ^{+0.82} _{-0.81}	1.19 ^{+0.35} _{-0.32}
12	EHE110304	55624.9548	116.37 ^{+0.73} _{-0.73}	-10.72 ^{+0.57} _{-0.65}
13	IC110514A	55695.0642	138.47 ^{+6.68} _{-3.78}	-1.94 ^{+0.97} _{-1.12}
14	DIF110521	55702.7666	235.13 ^{+2.70} _{-1.76}	20.30 ^{+1.00} _{-1.43}
15	IC110610A	55722.4261	272.55 ^{+1.67} _{-2.42}	35.64 ^{+1.30} _{-1.05}
16	IC110714A	55756.1130	68.20 ^{+0.31} _{-1.10}	40.67 ^{+0.44} _{-0.44}
17	DIF110722	55764.2196	315.66 ^{+5.91} _{-5.35}	5.29 ^{+4.85} _{-4.72}
18	IC110902A	55806.0922	9.76 ^{+2.85} _{-1.32}	7.59 ^{+0.87} _{-0.86}
19	IC110907A	55811.7946	196.08 ^{+3.92} _{-2.68}	9.40 ^{+1.56} _{-1.05}
20	DIF110930	55834.4451	266.48 ^{+2.09} _{-1.55}	-4.41 ^{+0.59} _{-0.86}
21	DIF111201	55896.8575	222.87 ^{+1.95} _{-1.95}	1.87 ^{+1.25} _{-1.18}
22	IC111216A	55911.2769	36.74 ^{+1.80} _{-2.24}	18.88 ^{+2.46} _{-2.82}
23	IC120301A	55987.8069	237.96 ^{+0.53} _{-0.61}	18.76 ^{+0.47} _{-0.51}
24	IC120515A	56062.9590	198.94 ^{+1.71} _{-1.41}	32.00 ^{+0.97} _{-1.09}
25	IC120523A	56070.5743	171.08 ^{+0.66} _{-1.41}	26.44 ^{+0.46} _{-0.37}
26	IC120807A	56146.2071	330.07 ^{+0.84} _{-0.83}	1.42 ^{+0.59} _{-0.45}
27	IC120916A	56186.3053	182.24 ^{+1.36} _{-1.71}	3.88 ^{+0.68} _{-0.82}
28	IC120922A	56192.5493	70.62 ^{+1.49} _{-1.27}	19.79 ^{+0.91} _{-0.71}
29	IC121011A	56211.7709	205.14 ^{+0.66} _{-0.71}	-2.28 ^{+0.53} _{-0.56}
30	IC121026A	56226.5995	169.80 ^{+1.32} _{-1.40}	27.91 ^{+0.85} _{-0.88}
31	IC130127A	56319.2800	352.97 ^{+1.32} _{-1.01}	-1.98 ^{+0.97} _{-0.89}
32	IC130408A	56390.1888	167.83 ^{+2.63} _{-3.96}	20.66 ^{+1.28} _{-0.99}
33	IC130627A	56470.1104	93.74 ^{+1.01} _{-1.15}	14.17 ^{+1.23} _{-1.04}
34	DIF130817	56521.8320	224.89 ^{+0.87} _{-1.19}	-4.44 ^{+1.21} _{-0.94}
35	IC130907A	56542.7931	130.17 ^{+0.48} _{-0.31}	-10.54 ^{+0.26} _{-0.30}
36	IC131014A	56579.9092	32.92 ^{+0.87} _{-0.71}	10.28 ^{+0.41} _{-0.57}
37	IC131023A	56588.5585	301.90 ^{+1.02} _{-1.05}	11.61 ^{+1.14} _{-1.30}
38	IC131124A	56620.1451	285.16 ^{+2.20} _{-1.54}	19.47 ^{+1.43} _{-1.46}
39	IC131204A	56630.4701	288.98 ^{+1.10} _{-0.83}	-14.21 ^{+0.77} _{-1.21}
40	IC140101A	56658.4039	192.26 ^{+2.07} _{-2.37}	-2.69 ^{+1.01} _{-0.71}
41	IC140108A	56665.3079	344.66 ^{+0.53} _{-0.48}	1.57 ^{+0.37} _{-0.34}
42	IC140109A	56666.5030	293.12 ^{+0.79} _{-1.19}	33.02 ^{+0.45} _{-0.53}
43	IC140203A	56691.7851	349.58 ^{+2.64} _{-2.54}	-13.55 ^{+1.14} _{-1.74}
44	DIF140522	56799.9614	349.39 ^{+2.89} _{-4.12}	18.05 ^{+1.94} _{-1.80}
45	IC140609A	56817.6364	106.26 ^{+2.68} _{-2.15}	1.31 ^{+1.04} _{-0.86}
46	IC140611A	56819.2044	110.65 ^{+0.53} _{-0.61}	11.45 ^{+0.19} _{-0.19}
47	IC140705A	56843.6687	25.88 ^{+1.85} _{-2.98}	2.54 ^{+0.79} _{-1.76}
48	IC140923A	56923.7211	169.72 ^{+0.70} _{-0.84}	-1.60 ^{+0.52} _{-0.30}
49	IC140927A	56927.1608	50.89 ^{+3.91} _{-5.14}	-0.63 ^{+1.49} _{-1.42}
50	IC150127A	57049.4813	100.37 ^{+1.36} _{-1.62}	4.59 ^{+0.79} _{-0.67}
51	IC150515A	57157.9416	91.49 ^{+0.93} _{-0.74}	12.14 ^{+0.53} _{-0.50}
52	IC150714A	57217.9097	326.29 ^{+1.50} _{-1.31}	26.36 ^{+1.89} _{-2.19}
53	IC150812B	57246.7591	328.27 ^{+0.75} _{-0.88}	6.17 ^{+0.48} _{-0.53}
54	IC150831A	57265.2178	54.76 ^{+0.92} _{-0.93}	34.00 ^{+1.14} _{-1.20}
55	IC150904A	57269.7597	133.77 ^{+0.53} _{-0.88}	28.08 ^{+0.51} _{-0.55}
56	IC150919A	57284.2057	279.54 ^{+1.75} _{-2.29}	30.35 ^{+2.18} _{-1.51}
57	IC150923A	57288.0268	103.23 ^{+0.70} _{-1.15}	3.96 ^{+0.60} _{-0.75}
58	IC150926A	57291.9012	194.55 ^{+0.79} _{-1.23}	-4.56 ^{+0.94} _{-0.63}
59	IC151017A	57312.6757	197.53 ^{+2.47} _{-2.72}	19.95 ^{+3.00} _{-2.29}
60	IC151114A	57340.8735	76.16 ^{+1.36} _{-1.37}	12.71 ^{+0.65} _{-0.72}
61	IC151122A	57348.5316	262.05 ^{+0.87} _{-1.06}	-2.24 ^{+0.64} _{-0.67}
62	IC160104A	57391.4438	79.41 ^{+0.83} _{-0.75}	5.00 ^{+0.87} _{-0.97}
63	IC160128A	57415.1835	263.76 ^{+1.10} _{-1.80}	-14.90 ^{+1.08} _{-1.20}
64	IC160225A	57443.8804	311.87 ^{+2.19} _{-1.77}	60.06 ^{+1.65} _{-1.38}
65	IC160331A	57478.5652	151.22 ^{+0.66} _{-0.66}	15.48 ^{+0.66} _{-0.73}
66	IC160510A	57518.6640	352.88 ^{+1.76} _{-1.45}	1.90 ^{+0.75} _{-0.67}

Table 3
(Continued)

Index	Track Name	Time (MJD)	R.A. (deg)	Decl. (deg)
67	EHE160731	57600.0799	214.50 ^{+0.75} _{-0.75}	-0.33 ^{+0.75} _{-0.75}
68	IC160806A	57606.5150	122.78 ^{+0.88} _{-1.23}	-0.71 ^{+0.56} _{-0.56}
69	IC160814A	57614.9069	200.04 ^{+3.12} _{-2.68}	-32.13 ^{+1.74} _{-1.25}
70	IC160924A	57655.7411	241.13 ^{+4.92} _{-5.89}	1.34 ^{+3.40} _{-2.79}
71	IC161001A	57662.4392	192.57 ^{+2.50} _{-2.07}	37.12 ^{+1.51} _{-2.48}
72	DIF161011	57672.0796	26.38 ^{+0.66} _{-0.66}	9.55 ^{+0.66} _{-0.66}
73	IC161012A	57673.6126	190.06 ^{+2.20} _{-4.04}	-7.48 ^{+2.18} _{-2.98}
74	IC161117A	57709.3320	78.66 ^{+1.85} _{-1.93}	1.60 ^{+1.91} _{-1.79}
75	IC161210A	57732.8380	46.36 ^{+2.38} _{-0.92}	15.25 ^{+0.93} _{-1.08}
76	IC170105A	57758.1419	309.95 ^{+5.01} _{-7.56}	8.16 ^{+2.00} _{-3.34}
77	IC170321A	57833.3141	98.26 ^{+1.32} _{-0.92}	-15.06 ^{+1.40} _{-1.20}
78	IC170514B	57887.3002	227.37 ^{+1.23} _{-1.10}	30.65 ^{+1.40} _{-0.67}
79	IC170626A	57930.5193	280.99 ^{+3.03} _{-1.63}	8.80 ^{+1.13} _{-0.90}
80	IC170704A	57938.2926	230.45 ^{+1.67} _{-1.71}	23.36 ^{+1.10} _{-0.89}
81	IC170717A	57951.8177	208.39 ^{+1.41} _{-1.19}	25.16 ^{+1.41} _{-1.35}
82	IC170803A	57968.0838	1.10 ^{+4.48} _{-1.76}	4.63 ^{+0.41} _{-0.41}
83	IC170809A	57974.5971	21.27 ^{+1.75} _{-1.06}	-2.28 ^{+0.60} _{-0.67}
84	IC170824A	57989.5538	41.92 ^{+3.04} _{-3.56}	12.37 ^{+1.45} _{-1.30}
85	IC170922A	58018.8712	77.43 ^{+1.14} _{-0.75}	5.79 ^{+0.64} _{-0.41}
86	IC170923A	58019.0213	173.45 ^{+2.38} _{-2.55}	-2.54 ^{+0.90} _{-1.30}
87	IC171015A	58041.0656	162.91 ^{+2.98} _{-1.72}	-15.48 ^{+1.62} _{-1.99}
88	IC171106A	58063.7775	340.14 ^{+0.61} _{-0.62}	7.44 ^{+0.31} _{-0.26}
89	IC180123A	58141.6771	77.12 ^{+2.51} _{-2.90}	8.01 ^{+0.41} _{-0.49}
90	IC180410A	58218.7768	218.50 ^{+0.79} _{-1.28}	0.56 ^{+0.75} _{-0.70}
91	IC180417A	58225.2785	305.73 ^{+3.60} _{-1.58}	-4.41 ^{+0.68} _{-0.74}
92	IC180908A	58369.8330	144.98 ^{+1.49} _{-2.20}	-2.39 ^{+1.16} _{-1.12}
93	IC181023A	58414.6927	270.18 ^{+1.89} _{-1.72}	-8.42 ^{+1.13} _{-1.55}
94	IC181120A	58442.7087	25.71 ^{+5.54} _{-5.28}	11.72 ^{+2.41} _{-4.50}
95	IC181121A	58443.5800	132.19 ^{+7.34} _{-6.99}	32.93 ^{+4.19} _{-3.57}
96	IC190124A	58507.1555	307.44 ^{+0.53} _{-1.14}	-32.22 ^{+0.96} _{-0.31}
97	IC190214A	58528.6727	228.25 ^{+0.79} _{-0.53}	-4.14 ^{+0.37} _{-0.30}
98	IC190221A	58535.3512	268.59 ^{+1.41} _{-1.58}	-17.00 ^{+1.25} _{-0.50}
99	IC190503A	58606.7244	120.19 ^{+0.66} _{-0.66}	6.43 ^{+0.68} _{-0.75}
100	IC190515A	58618.4506	127.88 ^{+0.79} _{-0.83}	12.60 ^{+0.49} _{-0.46}
101	IC190613A	58647.8294	312.19 ^{+0.66} _{-0.79}	26.57 ^{+0.75} _{-0.71}
102	IC190619A	58653.5516	343.52 ^{+4.13} _{-3.16}	10.28 ^{+2.01} _{-2.76}
103	IC190730A	58694.8685	226.14 ^{+1.28} _{-1.97}	10.77 ^{+1.03} _{-1.18}
104	IC190922A	58748.4047	167.30 ^{+2.81} _{-2.72}	-22.27 ^{+3.39} _{-3.30}
105	IC190922B	58748.9611	5.71 ^{+1.19} _{-1.27}	-1.53 ^{+0.90} _{-0.78}
106	IC191001A	58757.8398	313.99 ^{+6.94} _{-5.49}	12.79 ^{+1.65} _{-1.64}
107	IC191119A	58806.0427	229.31 ^{+5.49} _{-4.97}	3.77 ^{+2.47} _{-2.24}
108	IC200109A	58857.9873	165.45 ^{+3.61} _{-4.39}	11.80 ^{+1.18} _{-1.30}
109	IC200530A	58999.3295	255.37 ^{+2.46} _{-2.55}	26.61 ^{+2.32} _{-3.25}
110	IC200615A	59015.6176	142.95 ^{+1.15} _{-1.40}	3.66 ^{+1.16} _{-1.01}
111	IC200926A	59118.3293	96.46 ^{+0.70} _{-0.53}	-4.33 ^{+0.60} _{-0.75}
112	IC200929A	59121.7421	29.53 ^{+0.53} _{-0.53}	3.47 ^{+0.71} _{-0.34}
113	IC201007A	59129.9179	265.17 ^{+0.48} _{-0.49}	5.34 ^{+0.30} _{-0.19}
114	IC201114A	59167.6288	105.73 ^{+0.93} _{-1.27}	5.87 ^{+1.01} _{-1.05}
115	IC201115A	59168.0885	195.12 ^{+1.23} _{-1.45}	1.38 ^{+1.27} _{-1.08}
116	IC201130A	59183.8485	30.54 ^{+1.10} _{-1.27}	-12.10 ^{+1.14} _{-1.11}
117	IC201209A	59192.4276	6.86 ^{+1.01} _{-1.19}	-9.25 ^{+0.94} _{-1.10}
118	IC201221A	59204.5256	261.69 ^{+2.28} _{-2.46}	41.81 ^{+1.25} _{-1.14}
119	IC201222A	59205.0391	206.37 ^{+0.88} _{-0.75}	13.44 ^{+0.54} _{-0.35}
120	IC210210A	59255.4958	206.06 ^{+1.40} _{-0.95}	4.78 ^{+0.62} _{-0.56}
121	IC210811A	59437.0852	270.79 ^{+1.07} _{-1.08}	25.28 ^{+0.79} _{-0.84}
122	IC210922A	59479.7620	60.73 ^{+0.88} _{-0.61}	-4.18 ^{+0.37} _{-0.53}

Note. All alert events (track name starting with “IC”) and high-energy tracks (track name starting with “DIF” (selected from Abbasi et al. 2022b)), “EHE” (extremely high-energy), or “HESE” (high-energy-starting event) investigated in this this work. The track name includes the time of detection in the format yymmdd. In the case of alert events, the letter “A” or “B” is used to distinguish events detected on the same day. The time is the detection time in MJD, and R.A. and decl. list the best reconstruction coordinates with 90% confidence level uncertainties.

Appendix D Results Tables

Table 4 presents the results of the time-integrated point-source search, sorted by local significance. We list the best-fit values of our analysis (position, mean number of signal events,

spectral index) and the 90% confidence level upper flux limits with their respective valid energy ranges. Table 5 shows the results of the time-dependent analysis (also sorted by local significance) and the best-fit values for position, mean number of signal events, spectral index, and the respective best-fit time window for a single flare.

Table 4
Results of the Individual Time-integrated Analysis Sorted by Significance

Index	R.A. (deg)	Decl. (deg)	\hat{n}_S	$\hat{\gamma}$	p_{local}	$\Phi_{90\%100 \text{ TeV}}$ (TeV cm ² s) ⁻¹	$E_{\nu, \Phi, \text{min}}$ (TeV)	$E_{\nu, \Phi, \text{max}}$ (TeV)
13	137.87	-2.69	37.50	3.20	0.02	6.88×10^{-17}	0.9	483.1
106	318.48	11.88	13.38	2.08	0.03	9.00×10^{-17}	0.7	132.7
14	237.00	19.41	46.18	4.00	0.03	9.20×10^{-17}	0.7	88.3
2	298.74	11.74	38.86	4.00	0.04	8.95×10^{-17}	0.7	134.0
83	22.02	-2.13	28.76	2.93	0.04	5.00×10^{-17}	0.9	439.5
54	54.99	33.66	34.34	4.00	0.04	5.58×10^{-17}	0.7	50.8
16	68.36	40.82	4.48	1.71	0.05	7.31×10^{-17}	0.7	40.8
50	50.69	-0.44	43.72	4.00	0.06	5.77×10^{-17}	0.8	380.2
74	79.40	2.75	20.01	2.49	0.06	6.35×10^{-17}	0.8	293.8
10	284.83	3.32	16.71	2.38	0.07	7.66×10^{-17}	0.8	286.4
60	75.38	12.87	13.39	2.17	0.07	4.77×10^{-17}	0.7	118.6
23	237.76	19.08	37.66	4.00	0.07	6.31×10^{-17}	0.7	95.1
44	349.58	-13.17	12.27	2.64	0.07	6.17×10^{-17}	17.3	5093.3
25	171.74	26.44	11.18	2.31	0.07	6.01×10^{-17}	0.7	67.3
72	26.38	9.55	9.84	2.13	0.08	2.15×10^{-16}	0.8	158.1
45	350.01	19.02	40.34	3.91	0.10	7.68×10^{-17}	0.7	101.2
40	190.68	-2.35	26.39	4.00	0.11	4.11×10^{-17}	0.9	462.4
90	218.32	-0.15	32.53	3.49	0.11	4.22×10^{-17}	0.8	368.1
11	307.86	1.36	11.50	2.42	0.14	3.24×10^{-17}	0.8	353.2
93	269.42	-7.48	15.52	2.95	0.15	8.71×10^{-17}	2.2	2118.4
65	151.55	15.98	30.25	3.05	0.16	5.88×10^{-17}	0.7	105.0
77	99.20	-15.86	11.40	3.81	0.16	2.11×10^{-16}	22.7	6823.4
84	43.34	12.18	40.03	3.49	0.16	7.54×10^{-17}	0.7	131.2
85	77.43	5.38	16.73	2.54	0.17	4.18×10^{-17}	0.8	237.1
99	120.35	6.05	24.65	2.81	0.20	4.68×10^{-17}	0.8	223.4
55	133.77	27.71	22.04	4.00	0.20	3.85×10^{-17}	0.7	64.4
120	206.26	4.41	26.47	2.89	0.20	3.79×10^{-17}	0.8	265.5
4	141.25	47.32	17.24	2.61	0.21	7.67×10^{-17}	0.7	32.4
9	111.36	-0.37	25.89	4.00	0.21	2.89×10^{-17}	0.8	371.5
81	208.19	25.69	5.14	1.86	0.22	5.56×10^{-17}	0.7	65.9
28	70.62	19.43	8.08	2.09	0.22	4.92×10^{-17}	0.7	86.5
15	273.27	36.20	22.40	2.72	0.22	6.14×10^{-17}	0.7	43.9
30	171.12	27.73	32.96	3.94	0.23	5.37×10^{-17}	0.7	62.2
31	353.91	-1.20	20.58	2.65	0.24	3.11×10^{-17}	0.9	394.5
18	9.38	7.59	5.54	2.09	0.24	4.38×10^{-17}	0.8	181.1
115	194.76	2.47	17.33	2.48	0.26	2.81×10^{-17}	0.8	300.6
33	93.74	14.17	18.68	2.58	0.26	3.76×10^{-17}	0.7	116.7
113	265.17	5.15	21.84	4.00	0.28	4.00×10^{-17}	0.8	248.3
47	27.54	2.74	36.77	3.79	0.28	3.52×10^{-17}	0.8	293.8
34	225.59	-4.09	14.38	2.78	0.30	3.24×10^{-17}	1.0	642.7
119	206.90	13.27	20.54	3.16	0.30	3.12×10^{-17}	0.7	118.6
112	29.35	3.30	22.47	3.12	0.30	3.70×10^{-17}	0.8	281.2
114	104.46	6.38	28.34	3.01	0.30	2.82×10^{-17}	0.8	224.4
94	26.90	7.81	47.41	4.00	0.30	7.00×10^{-17}	0.8	170.6
7	330.73	11.10	21.11	2.90	0.31	3.57×10^{-17}	0.7	134.0
56	277.48	29.41	25.41	2.83	0.32	2.86×10^{-17}	0.7	55.0
75	46.95	15.99	32.99	3.15	0.32	4.65×10^{-17}	0.7	106.7
59	195.23	20.14	8.95	2.09	0.33	6.66×10^{-17}	0.7	83.0
79	283.21	9.37	32.19	3.43	0.33	5.19×10^{-17}	0.8	167.1
78	227.78	30.25	28.65	4.00	0.33	6.23×10^{-17}	0.7	54.3
122	60.27	-3.99	6.55	4.00	0.34	5.41×10^{-17}	1.0	619.4
52	91.86	12.32	23.31	3.25	0.34	3.58×10^{-17}	0.7	130.0
86	171.49	-2.36	8.32	2.19	0.34	3.72×10^{-17}	0.9	467.7
49	168.88	-1.43	20.41	4.00	0.35	2.03×10^{-17}	0.9	409.3
109	255.82	26.80	26.23	2.85	0.36	2.66×10^{-17}	0.7	67.8
88	340.75	7.44	19.33	4.00	0.37	8.03×10^{-17}	0.8	187.5

Table 4
(Continued)

Index	R.A. (deg)	Decl. (deg)	\hat{n}_S	$\hat{\gamma}$	P_{local}	$\Phi_{90\%100\text{ TeV}}$ (TeV cm ² s) ⁻¹	$E_{\nu,\Phi,\min}$ (TeV)	$E_{\nu,\Phi,\max}$ (TeV)
70	237.60	1.14	41.83	4.00	0.38	4.43×10^{-17}	0.8	334.2
87	164.10	-14.76	11.78	3.90	0.39	5.17×10^{-17}	20.7	6368.0
46	105.48	1.66	25.18	2.74	0.40	1.73×10^{-16}	0.8	320.6
102	343.52	9.69	42.18	3.38	0.40	2.69×10^{-17}	0.7	158.9
66	354.25	1.40	27.02	4.00	0.41	2.40×10^{-17}	0.8	338.1
92	144.38	-3.14	18.45	4.00	0.42	2.90×10^{-17}	0.9	517.6
100	128.67	12.76	5.42	2.18	0.43	3.28×10^{-17}	0.7	123.0
110	143.14	3.32	21.32	2.82	0.46	3.36×10^{-17}	0.8	281.2
97	228.84	-3.96	6.79	4.00	0.46	3.30×10^{-17}	1.0	620.9
91	304.94	-4.97	12.09	4.00	0.47	1.34×10^{-16}	1.1	871.0
63	264.13	-15.07	8.15	3.88	0.47	4.46×10^{-17}	21.1	6295.1
101	312.19	25.86	7.93	2.24	0.47	1.57×10^{-16}	0.7	68.9
98	269.80	-16.11	9.81	3.67	0.47	4.83×10^{-17}	23.3	6982.3
108	167.45	12.39	31.98	3.15	0.48	5.15×10^{-17}	0.7	127.1
5	306.96	19.44	15.41	2.38	0.49	4.10×10^{-17}	0.7	86.9
26	329.57	1.82	19.70	4.00	0.49	1.85×10^{-17}	0.8	308.3
68	122.25	-0.34	18.24	3.96	0.51	2.00×10^{-17}	0.8	380.2
37	301.20	10.50	5.10	2.17	0.51	3.23×10^{-17}	0.7	140.9
41	344.50	1.94	4.08	2.21	0.52	2.54×10^{-17}	0.8	309.0
27	180.72	3.55	19.65	3.14	0.55	2.43×10^{-17}	0.8	291.7
69	200.71	-31.94	9.69	3.55	0.57	2.51×10^{-17}	61.9	11,967.4
117	5.67	-9.06	7.22	2.95	0.57	4.89×10^{-16}	5.5	2944.4
51	99.29	4.59	23.19	3.09	0.57	6.52×10^{-17}	0.8	251.2
6	266.87	13.40	9.33	2.66	0.57	3.08×10^{-17}	0.7	118.3
39	289.16	-14.21	6.66	3.15	0.59	9.48×10^{-17}	19.1	5701.6
64	312.60	59.86	9.68	2.06	0.59	8.38×10^{-17}	0.6	23.8
73	187.17	-6.89	9.57	2.26	0.61	4.64×10^{-17}	1.6	1706.1
25	199.80	32.58	16.22	2.75	0.61	7.43×10^{-17}	0.7	51.9
80	230.24	23.91	16.44	2.66	0.62	4.83×10^{-17}	0.7	64.9
105	4.80	-1.92	16.74	2.82	0.62	2.82×10^{-17}	0.9	424.6
61	261.34	-2.58	9.54	2.82	0.67	2.46×10^{-17}	0.9	460.3
104	166.88	-20.47	5.88	2.16	0.68	2.72×10^{-17}	36.8	8851.2
22	37.34	18.88	27.49	3.83	0.70	2.80×10^{-16}	0.7	101.9
32	169.25	20.84	22.64	2.87	0.71	4.67×10^{-17}	0.7	79.4
107	233.04	3.02	35.13	3.54	0.73	4.45×10^{-17}	0.8	281.8
118	263.47	42.52	6.25	1.99	0.74	4.06×10^{-17}	0.7	40.2
58	193.67	-3.81	6.84	4.00	0.74	3.21×10^{-17}	1.0	588.8
20	266.48	-5.10	9.66	3.55	0.74	6.92×10^{-17}	1.1	948.4
116	30.72	-11.91	6.42	3.38	0.76	3.81×10^{-17}	13.6	4786.3
12	115.64	-10.72	1.53	2.35	0.76	4.62×10^{-17}	10.7	4064.4
95	127.53	35.53	26.45	2.65	0.77	9.04×10^{-17}	0.7	47.3
3	347.90	22.20	33.17	4.00	0.79	8.66×10^{-17}	0.7	78.2
121	270.36	25.11	13.05	4.00	0.79	4.86×10^{-17}	0.7	68.2
38	284.97	19.11	19.88	4.00	0.80	3.57×10^{-16}	0.7	94.0
52	326.72	27.30	7.78	2.44	0.80	4.65×10^{-17}	0.7	62.8
89	79.63	8.01	19.75	4.00	0.81	4.12×10^{-17}	0.8	166.7
96	307.97	-32.03	2.48	2.49	0.81	3.93×10^{-17}	61.5	12,416.5
47	110.83	11.45	4.77	3.57	0.82	6.09×10^{-17}	0.7	136.8
57	103.41	3.96	2.01	2.14	0.82	3.55×10^{-17}	0.8	281.8
62	79.41	5.00	12.34	3.04	0.83	2.81×10^{-17}	0.8	260.0
42	293.71	33.32	7.76	2.89	0.83	2.83×10^{-17}	0.7	48.3
82	4.61	4.36	16.46	4.00	0.85	3.26×10^{-17}	0.8	272.3
19	194.36	9.59	25.50	4.00	0.86	4.15×10^{-17}	0.7	158.1
103	225.75	10.77	12.59	2.88	0.88	2.55×10^{-17}	0.7	141.6
36	33.79	10.09	2.16	2.01	0.91	4.01×10^{-17}	0.8	158.9
76	310.75	9.07	9.19	2.17	0.93	3.58×10^{-17}	0.7	165.6
21	222.47	0.89	17.33	3.34	0.94	2.55×10^{-17}	0.8	342.8
67	214.31	-0.89	8.92	3.32	0.94	5.71×10^{-17}	0.8	363.1
71	193.07	37.50	14.94	3.19	0.94	3.45×10^{-17}	0.7	42.6
17	314.47	8.39	30.90	3.32	0.99	7.36×10^{-17}	0.8	171.0
111	96.46	-5.08	0.55	3.35	1.00	2.74×10^{-17}	1.1	924.7
53	327.74	5.82	1.69	3.75	1.00	4.50×10^{-17}	0.8	229.1

Table 4
(Continued)

Index	R.A. (deg)	Decl. (deg)	\hat{n}_S	$\hat{\gamma}$	p_{local}	$\Phi_{90\%100\text{ TeV}}$ (TeV cm ² s) ⁻¹	$E_{\nu,\Phi,\text{min}}$ (TeV)	$E_{\nu,\Phi,\text{max}}$ (TeV)
29	204.43	-2.47	0.00	2.56	1.00	1.87×10^{-17}	0.9	465.6
1	29.32	1.12	0.00	2.83	1.00	1.83×10^{-17}	0.8	333.4
8	88.31	0.33	0.00	3.20	1.00	2.04×10^{-17}	0.8	376.7
35	130.01	-10.69	0.00	1.50	1.00	5.02×10^{-17}	10.6	4083.2

Note. The first column contains the index of the alert+ event as in Table 3. The second and third columns list the best-fit position of this work. The fourth and fifth columns contain the best-fit parameter of the likelihood optimization \hat{n}_S and $\hat{\gamma}$. The sixth column shows the local p -values, and the seventh column shows the 90% confidence level upper flux limits. The central 90% quantiles of the neutrino energies of the detected simulated events for computing the flux limit are listed in the eighth and ninth columns. They define the range in which the flux limit is valid. The global p -value for the time-integrated single-source search is 0.98.

Table 5
Results of the Time-dependent Analysis Sorted by Significance

Index	R.A. (deg)	Decl. (deg)	\hat{n}_S	$\hat{\gamma}$	$\hat{\mu}_T$	$\hat{\sigma}_T$	p_{local}
85	77.43	5.38	11.98	2.31	57001	64	1.4×10^{-3}
107	227.72	5.10	9.48	2.38	57774	9	1.6×10^{-2}
17	318.42	1.75	10.41	2.45	57008	20	1.7×10^{-2}
60	75.77	13.20	5.19	2.07	58155	10	1.9×10^{-2}
33	93.74	14.35	14.45	2.96	57078	39	2.1×10^{-2}
30	169.60	28.76	8.52	3.04	56153	5	2.5×10^{-2}
83	21.27	-2.95	18.44	2.90	57186	236	3.4×10^{-2}
120	206.26	4.41	19.76	3.02	57427	103	5.1×10^{-2}
99	120.19	5.87	12.71	2.68	56267	51	5.5×10^{-2}
87	164.10	-17.07	8.10	3.80	58493	94	7.3×10^{-2}
47	24.89	1.56	11.01	2.70	57764	22	7.8×10^{-2}
23	238.14	18.42	8.52	3.03	57173	5	8.3×10^{-2}
90	217.59	0.03	9.40	2.55	57646	29	8.4×10^{-2}
104	165.83	-23.82	6.90	3.12	58904	20	8.6×10^{-2}
11	307.86	1.36	3.16	2.04	57056	7	9.5×10^{-2}
27	180.53	3.88	13.77	3.69	56470	26	9.6×10^{-2}
101	312.19	26.04	4.81	2.65	58692	5	0.10
100	127.71	12.14	7.16	2.61	57214	5	0.11
44	350.80	-14.90	5.34	3.08	57862	13	0.11
12	115.82	-10.53	4.32	2.61	58701	19	0.11
52	326.72	27.49	5.81	1.91	57677	5	0.11
115	194.94	1.74	5.59	2.61	58529	6	0.12
6	266.87	13.40	6.67	2.39	55551	37	0.12
36	33.62	9.90	4.87	1.98	55815	10	0.12
25	171.74	26.44	11.23	2.67	58063	120	0.12
73	188.33	-6.10	9.37	2.68	56698	78	0.12
16	68.36	40.82	3.93	1.66	58434	23	0.13
4	141.48	47.48	20.87	2.54	57931	268	0.13
50	48.32	0.49	17.16	3.53	55870	52	0.19
52	91.68	12.14	10.51	3.43	57694	12	0.20
2	298.56	11.55	8.18	2.67	56998	13	0.22
108	168.46	11.80	7.88	2.61	57075	7	0.23
103	226.14	10.77	5.93	2.55	55500	9	0.25
109	255.82	27.00	13.24	2.92	58940	32	0.25
28	70.81	19.08	8.34	2.85	58293	12	0.25
7	331.46	10.71	11.97	3.13	57753	18	0.26
105	4.80	-0.81	10.26	2.77	57854	21	0.28
74	77.50	2.55	12.44	2.49	57407	144	0.29
34	224.10	-4.09	5.26	4.00	56352	17	0.32
5	306.55	19.63	10.43	2.84	57728	37	0.33
121	271.00	25.11	18.65	4.00	56858	125	0.33
54	54.06	34.00	5.54	2.38	55465	8	0.34
78	227.37	30.25	7.27	4.00	56554	6	0.34
110	142.35	2.82	9.97	3.29	57011	10	0.34
113	265.01	5.34	11.57	2.66	58747	137	0.35

Table 5
(Continued)

Index	R.A. (deg)	Decl. (deg)	\hat{n}_S	$\hat{\gamma}$	$\hat{\mu}_T$	$\hat{\sigma}_T$	P_{local}
62	79.41	5.00	8.33	2.77	55881	23	0.36
51	100.95	4.98	13.56	2.74	57683	43	0.36
59	195.23	19.76	5.95	1.95	57777	43	0.37
72	26.38	9.71	2.64	1.83	55869	20	0.38
3	347.47	24.93	19.50	4.00	58817	67	0.39
40	193.20	-3.22	4.72	3.27	56069	5	0.39
61	261.34	-2.58	2.18	2.23	56311	5	0.40
47	110.83	11.64	3.10	2.01	56284	5	0.40
86	173.25	-2.54	5.89	3.94	58914	8	0.40
31	353.16	-1.40	4.50	2.61	57485	5	0.41
106	317.26	12.24	10.38	2.17	55648	194	0.42
69	200.71	-31.94	9.17	2.68	57641	149	0.46
81	207.80	26.04	6.19	2.04	57909	35	0.47
8	88.50	0.46	3.75	4.00	58729	5	0.47
35	130.17	-10.28	1.97	3.46	55727	5	0.48
37	301.37	10.50	4.16	2.06	56186	59	0.48
32	166.79	21.76	17.27	3.06	58039	105	0.48
26	329.40	1.12	10.31	4.00	57346	20	0.49
96	307.97	-32.03	5.75	2.71	58223	130	0.49
55	133.55	27.71	12.73	4.00	57202	96	0.49
65	151.05	14.93	10.71	2.69	56073	74	0.50
102	341.35	11.01	23.55	3.50	55932	225	0.50
53	327.92	5.82	7.41	3.54	57307	5	0.51
10	284.83	3.32	2.92	1.95	58860	51	0.52
1	29.51	1.23	4.52	4.00	58152	5	0.52
97	228.25	-4.44	4.67	4.00	57925	23	0.54
18	9.38	7.59	2.45	1.76	56920	133	0.55
114	105.55	6.38	10.56	3.26	57438	73	0.55
98	268.20	-16.29	8.79	3.93	55171	32	0.56
75	47.55	15.44	6.99	2.85	56015	6	0.56
19	199.21	8.87	9.84	3.33	58512	16	0.58
21	223.65	1.67	6.06	2.04	57754	58	0.59
46	105.67	0.97	8.75	2.52	56044	62	0.60
49	168.88	-1.43	12.14	4.00	57034	135	0.60
88	340.60	7.59	6.69	4.00	56225	10	0.63
122	60.12	-3.99	4.24	4.00	57539	33	0.64
20	266.67	-5.10	9.44	3.81	57444	122	0.65
79	282.81	8.26	16.67	2.98	57871	144	0.66
92	144.78	-2.95	12.23	4.00	58406	95	0.67
91	307.53	-4.97	6.03	2.39	57105	26	0.68
95	130.33	36.92	10.91	4.00	55469	51	0.68
82	359.34	4.36	11.18	3.54	56650	26	0.68
80	230.45	23.54	8.44	2.91	56927	13	0.68
112	29.00	3.47	3.64	4.00	57045	5	0.69
93	270.56	-7.29	6.61	2.10	58532	44	0.69
70	237.20	1.14	16.00	3.27	56123	65	0.70
22	37.14	18.69	16.67	2.89	57494	112	0.73
66	354.64	1.73	4.05	2.30	57815	5	0.73
119	207.07	13.27	6.99	3.26	56078	20	0.74
25	199.80	32.58	6.94	2.41	55763	38	0.74
39	289.35	-15.33	3.13	3.60	58116	8	0.75
63	263.76	-15.07	5.68	3.72	57964	136	0.76
15	272.55	36.20	5.39	1.97	55850	40	0.76
57	102.85	3.77	5.77	4.00	57412	5	0.77
77	97.34	-15.06	2.86	3.94	57966	5	0.79
111	96.46	-5.08	3.54	3.78	55790	14	0.80
117	6.66	-9.98	9.12	3.27	55227	69	0.82
94	25.91	7.61	24.88	3.40	56859	99	0.82
84	39.94	13.64	23.44	4.00	58516	221	0.83
14	235.34	19.76	10.65	2.42	58482	76	0.84
58	194.20	-3.81	6.96	2.76	55443	224	0.84
89	77.12	7.68	4.52	4.00	57329	5	0.84
76	310.55	6.39	9.45	2.80	55956	23	0.85


























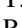



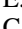



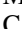


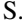


Table 5
(Continued)










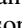






















Index	R.A. (deg)	Decl. (deg)	\hat{n}_s	$\hat{\gamma}$	$\hat{\mu}_T$	$\hat{\sigma}_T$	P_{local}
67	214.12	-0.71	6.49	3.58	57509	22	0.87
29	205.30	-2.65	6.59	3.19	56484	7	0.87
64	312.23	60.79	5.30	2.32	56903	7	0.88
13	137.87	-2.87	20.28	3.26	57963	386	0.90
9	111.16	-0.21	6.61	2.97	58059	19	0.90
68	122.43	-1.08	9.92	3.52	55389	127	0.91
56	280.64	30.35	12.20	2.57	57865	153	0.91
116	30.54	-11.15	3.03	2.49	57403	5	0.93
41	345.19	1.40	8.92	3.69	55980	35	0.93
42	293.51	33.32	4.21	4.00	56102	5	0.94
38	287.16	19.47	10.07	4.00	55637	45	0.96
45	346.71	18.24	12.32	2.61	55259	143	0.97
118	263.21	42.52	6.51	3.44	56064	6	0.98
71	191.42	35.21	4.87	1.60	55301	42	0.99

Note. The first column contains the alert+ index as in Table 3. The second and third columns list the best-fit position. The fourth and fifth columns contain the best-fit parameter of the likelihood optimizations n_s and γ . The sixth and seventh columns list the best-fit results for the Gaussian time window with mean μ_T and width σ_T . The eighth column shows the local p -values. The global p -value for the time-dependent analysis is 0.156.

ORCID iDs

- R. Abbasi <https://orcid.org/0000-0001-6141-4205>
M. Ackermann <https://orcid.org/0000-0001-8952-588X>
S. K. Agarwalla <https://orcid.org/0000-0002-9714-8866>
J. A. Aguilar <https://orcid.org/0000-0003-2252-9514>
M. Ahlers <https://orcid.org/0000-0003-0709-5631>
J. M. Alameddine <https://orcid.org/0000-0002-9534-9189>
K. Andeen <https://orcid.org/0000-0001-9394-0007>
G. Anton <https://orcid.org/0000-0003-2039-4724>
C. Argüelles <https://orcid.org/0000-0003-4186-4182>
S. N. Axani <https://orcid.org/0000-0001-8866-3826>
X. Bai <https://orcid.org/0000-0002-1827-9121>
A. Balagopal V. <https://orcid.org/0000-0001-5367-8876>
S. W. Barwick <https://orcid.org/0000-0003-2050-6714>
V. Basu <https://orcid.org/0000-0002-9528-2009>
J. J. Beatty <https://orcid.org/0000-0003-0481-4952>
J. Becker Tjus <https://orcid.org/0000-0002-1748-7367>
J. Beise <https://orcid.org/0000-0002-7448-4189>
C. Bellenghi <https://orcid.org/0000-0001-8525-7515>
S. BenZvi <https://orcid.org/0000-0001-5537-4710>
E. Bernardini <https://orcid.org/0000-0003-3108-1141>
D. Z. Besson <https://orcid.org/0000-0001-6733-963X>
E. Blaufuss <https://orcid.org/0000-0001-5450-1757>
S. Blot <https://orcid.org/0000-0003-1089-3001>
J. Y. Book <https://orcid.org/0000-0001-6687-5959>
C. Boscolo Meneguolo <https://orcid.org/0000-0001-8325-4329>
S. Böser <https://orcid.org/0000-0002-5918-4890>
O. Botner <https://orcid.org/0000-0001-8588-7306>
J. Böttcher <https://orcid.org/0000-0002-3387-4236>
B. Brinson <https://orcid.org/0000-0001-9128-1159>
M. A. Campana <https://orcid.org/0000-0003-4162-5739>
C. Chen <https://orcid.org/0000-0002-8139-4106>
Z. Chen <https://orcid.org/0000-0002-2813-7688>
D. Chirkin <https://orcid.org/0000-0003-4911-1345>
B. A. Clark <https://orcid.org/0000-0003-4089-2245>
A. Coleman <https://orcid.org/0000-0003-1510-1712>
J. M. Conrad <https://orcid.org/0000-0002-6393-0438>
P. Coppin <https://orcid.org/0000-0001-6869-1280>
P. Correa <https://orcid.org/0000-0002-1158-6735>
D. F. Cowen <https://orcid.org/0000-0003-4738-0787>
P. Dave <https://orcid.org/0000-0002-3879-5115>
C. De Clercq <https://orcid.org/0000-0001-5266-7059>
J. J. DeLaunay <https://orcid.org/0000-0001-5229-1995>
D. Delgado <https://orcid.org/0000-0002-4306-8828>
A. Desai <https://orcid.org/0000-0001-7405-9994>
P. Desiati <https://orcid.org/0000-0001-9768-1858>
K. D. de Vries <https://orcid.org/0000-0002-9842-4068>
G. de Wasseige <https://orcid.org/0000-0002-1010-5100>
T. DeYoung <https://orcid.org/0000-0003-4873-3783>
A. Diaz <https://orcid.org/0000-0001-7206-8336>
J. C. Díaz-Vélez <https://orcid.org/0000-0002-0087-0693>
H. Dujmovic <https://orcid.org/0000-0003-1891-0718>
M. A. DuVernois <https://orcid.org/0000-0002-2987-9691>
P. Eller <https://orcid.org/0000-0001-6354-5209>
D. Elsässer <https://orcid.org/0000-0001-6796-3205>
H. Erpenbeck <https://orcid.org/0000-0001-6319-2108>
P. A. Evenson <https://orcid.org/0000-0001-7929-810X>
K. L. Fan <https://orcid.org/0000-0002-8246-4751>
A. R. Fazely <https://orcid.org/0000-0002-6907-8020>
A. Fedynitch <https://orcid.org/0000-0003-2837-3477>
C. Finley <https://orcid.org/0000-0003-3350-390X>
L. Fischer <https://orcid.org/0000-0002-7645-8048>
D. Fox <https://orcid.org/0000-0002-3714-672X>
A. Franckowiak <https://orcid.org/0000-0002-5605-2219>
E. Ganster <https://orcid.org/0000-0003-4393-6944>
A. Garcia <https://orcid.org/0000-0002-8186-2459>
A. Ghadimi <https://orcid.org/0000-0002-6350-6485>
C. Glaser <https://orcid.org/0000-0001-5998-2553>
T. Glauch <https://orcid.org/0000-0003-1804-4055>
T. Glüsenskamp <https://orcid.org/0000-0002-2268-9297>
S. Goswami <https://orcid.org/0000-0002-0373-9770>
S. J. Gray <https://orcid.org/0000-0003-2907-8306>
S. Griffin <https://orcid.org/0000-0002-0779-9623>

- S. Griswold  <https://orcid.org/0000-0002-7321-7513>
K. M. Groth  <https://orcid.org/0000-0002-1581-9049>
P. Gutjahr  <https://orcid.org/0000-0001-7980-7285>
A. Hallgren  <https://orcid.org/0000-0001-7751-4489>
L. Halve  <https://orcid.org/0000-0003-2237-6714>
F. Halzen  <https://orcid.org/0000-0001-6224-2417>
H. Hamdaoui  <https://orcid.org/0000-0001-5709-2100>
A. Haungs  <https://orcid.org/0000-0002-9638-7574>
K. Helbing  <https://orcid.org/0000-0003-2072-4172>
F. Henningsen  <https://orcid.org/0000-0002-0680-6588>
N. Heyer  <https://orcid.org/0000-0001-9036-8623>
C. Hill  <https://orcid.org/0000-0003-0647-9174>
W. Hou  <https://orcid.org/0000-0003-3422-7185>
T. Huber  <https://orcid.org/0000-0002-6515-1673>
K. Hultqvist  <https://orcid.org/0000-0003-0602-9472>
M. Hünnefeld  <https://orcid.org/0000-0002-2827-6522>
G. S. Japaridze  <https://orcid.org/0000-0002-7000-5291>
M. Jeong  <https://orcid.org/0000-0003-2420-6639>
M. Jin  <https://orcid.org/0000-0003-0487-5595>
B. J. P. Jones  <https://orcid.org/0000-0003-3400-8986>
D. Kang  <https://orcid.org/0000-0002-5149-9767>
W. Kang  <https://orcid.org/0000-0003-3980-3778>
A. Kappes  <https://orcid.org/0000-0003-1315-3711>
T. Karg  <https://orcid.org/0000-0003-3251-2126>
M. Karl  <https://orcid.org/0000-0003-2475-8951>
A. Karle  <https://orcid.org/0000-0001-9889-5161>
U. Katz  <https://orcid.org/0000-0002-7063-4418>
M. Kauer  <https://orcid.org/0000-0003-1830-9076>
J. L. Kelley  <https://orcid.org/0000-0002-0846-4542>
A. Khatee Zathul  <https://orcid.org/0000-0002-8735-8579>
A. Kheirandish  <https://orcid.org/0000-0001-7074-0539>
J. Kiryluk  <https://orcid.org/0000-0003-0264-3133>
S. R. Klein  <https://orcid.org/0000-0003-2841-6553>
A. Kochocki  <https://orcid.org/0000-0003-3782-0128>
R. Koirala  <https://orcid.org/0000-0002-7735-7169>
H. Kolanoski  <https://orcid.org/0000-0003-0435-2524>
T. Kontrimas  <https://orcid.org/0000-0001-8585-0933>
L. Köpke  <https://orcid.org/0000-0001-8530-6348>
C. Kopper  <https://orcid.org/0000-0001-6288-7637>
D. J. Koskinen  <https://orcid.org/0000-0002-0514-5917>
P. Koundal  <https://orcid.org/0000-0002-5917-5230>
M. Kovacevich  <https://orcid.org/0000-0002-5019-5745>
M. Kowalski  <https://orcid.org/0000-0001-8594-8666>
J. Krishnamoorthi  <https://orcid.org/0009-0006-1352-2248>
A. Kumar  <https://orcid.org/0000-0002-8367-8401>
N. Kurahashi  <https://orcid.org/0000-0003-1047-8094>
N. Lad  <https://orcid.org/0000-0001-9302-5140>
C. Lagunas Gualda  <https://orcid.org/0000-0002-9040-7191>
M. Lamoureux  <https://orcid.org/0000-0002-8860-5826>
M. J. Larson  <https://orcid.org/0000-0002-6996-1155>
F. Lauber  <https://orcid.org/0000-0001-5648-5930>
J. P. Lazar  <https://orcid.org/0000-0003-0928-5025>
J. W. Lee  <https://orcid.org/0000-0001-5681-4941>
K. Leonard DeHolton  <https://orcid.org/0000-0002-8795-0601>
A. Leszczyńska  <https://orcid.org/0000-0003-0935-6313>
M. Lincetto  <https://orcid.org/0000-0002-1460-3369>
Q. R. Liu  <https://orcid.org/0000-0003-3379-6423>
E. Lohfink  <https://orcid.org/0000-0003-3248-5682>
L. Lu  <https://orcid.org/0000-0003-3175-7770>
F. Lucarelli  <https://orcid.org/0000-0002-9558-8788>
W. Luszczak  <https://orcid.org/0000-0003-3085-0674>
Y. Lyu  <https://orcid.org/0000-0002-2333-4383>
J. Madsen  <https://orcid.org/0000-0003-2415-9959>
E. Manao  <https://orcid.org/0009-0002-6197-8574>
I. C. Mariş  <https://orcid.org/0000-0002-5771-1124>
R. Maruyama  <https://orcid.org/0000-0003-2794-512X>
F. Mayhew  <https://orcid.org/0000-0001-7609-403X>
F. McNally  <https://orcid.org/0000-0002-0785-2244>
K. Meagher  <https://orcid.org/0000-0003-3967-1533>
M. Meier  <https://orcid.org/0000-0002-9483-9450>
L. Merten  <https://orcid.org/0000-0003-1332-9895>
T. Montaruli  <https://orcid.org/0000-0001-5014-2152>
R. W. Moore  <https://orcid.org/0000-0003-4160-4700>
M. Moulai  <https://orcid.org/0000-0001-7909-5812>
R. Naab  <https://orcid.org/0000-0003-2512-466X>
R. Nagai  <https://orcid.org/0000-0001-7503-2777>
J. Necker  <https://orcid.org/0000-0003-0280-7484>
H. Niederhausen  <https://orcid.org/0000-0002-9566-4904>
M. U. Nisa  <https://orcid.org/0000-0002-6859-3944>
S. C. Nowicki  <https://orcid.org/0000-0003-2497-8057>
A. Obertacke Pollmann  <https://orcid.org/0000-0002-2492-043X>
B. Oeyen  <https://orcid.org/0000-0003-2940-3164>
E. O'Sullivan  <https://orcid.org/0000-0003-1882-8802>
H. Pandya  <https://orcid.org/0000-0002-6138-4808>
N. Park  <https://orcid.org/0000-0002-4282-736X>
E. N. Paudel  <https://orcid.org/0000-0001-9276-7994>
C. Pérez de los Heros  <https://orcid.org/0000-0002-2084-5866>
J. Peterson  <https://orcid.org/0000-0002-7985-1443>
S. Philippen  <https://orcid.org/0000-0002-0276-0092>
A. Pizzuto  <https://orcid.org/0000-0002-8466-8168>
M. Plum  <https://orcid.org/0000-0001-8691-242X>
B. Pries  <https://orcid.org/0000-0003-4811-9863>
C. Raab  <https://orcid.org/0000-0001-9921-2668>
A. Rehman  <https://orcid.org/0000-0001-7616-5790>
E. Resconi  <https://orcid.org/0000-0003-0705-2770>
S. Reusch  <https://orcid.org/0000-0002-7788-628X>
W. Rhode  <https://orcid.org/0000-0003-2636-5000>
B. Riedel  <https://orcid.org/0000-0002-9524-8943>
M. Rongen  <https://orcid.org/0000-0002-7057-1007>
C. Rott  <https://orcid.org/0000-0002-6958-6033>
T. Ruhe  <https://orcid.org/0000-0002-4080-9563>
D. Ryckbosch  <https://orcid.org/0000-0002-8759-7553>
I. Safa  <https://orcid.org/0000-0001-8737-6825>
D. Salazar-Gallegos  <https://orcid.org/0000-0002-9312-9684>
A. Sandrock  <https://orcid.org/0000-0002-6779-1172>
M. Santander  <https://orcid.org/0000-0001-7297-8217>
S. Sarkar  <https://orcid.org/0000-0002-1206-4330>
S. Sarkar  <https://orcid.org/0000-0002-3542-858X>
H. Schieler  <https://orcid.org/0000-0002-2637-4778>
S. Schindler  <https://orcid.org/0000-0001-5507-8890>
L. Schlickmann  <https://orcid.org/0000-0002-9746-6872>
F. Schlüter  <https://orcid.org/0000-0002-5545-4363>
J. Schneider  <https://orcid.org/0000-0001-7752-5700>
F. G. Schröder  <https://orcid.org/0000-0001-8495-7210>
L. Schumacher  <https://orcid.org/0000-0001-8945-6722>
S. Sclafani  <https://orcid.org/0000-0001-9446-1219>
S. Seunarine  <https://orcid.org/0000-0003-3272-6896>
M. Silva  <https://orcid.org/0000-0001-6940-8184>
B. Skrzypek  <https://orcid.org/0000-0002-0910-1057>
B. Smithers  <https://orcid.org/0000-0003-1273-985X>
J. Soedingrekso  <https://orcid.org/0000-0003-1011-2797>

D. Soldin  <https://orcid.org/0000-0003-3005-7879>
 G. Sommani  <https://orcid.org/0000-0002-0094-826X>
 G. M. Spiczak  <https://orcid.org/0000-0002-0030-0519>
 C. Spiering  <https://orcid.org/0000-0001-7372-0074>
 T. Stezelberger  <https://orcid.org/0000-0003-2676-9574>
 T. Stuttard  <https://orcid.org/0000-0001-7944-279X>
 G. W. Sullivan  <https://orcid.org/0000-0002-2585-2352>
 I. Taboada  <https://orcid.org/0000-0003-3509-3457>
 S. Ter-Antonyan  <https://orcid.org/0000-0002-5788-1369>
 W. G. Thompson  <https://orcid.org/0000-0003-2988-7998>
 J. Thwaites  <https://orcid.org/0000-0001-9179-3760>
 K. Tollefson  <https://orcid.org/0000-0001-9725-1479>
 S. Toscano  <https://orcid.org/0000-0002-1860-2240>
 A. Trettin  <https://orcid.org/0000-0003-0350-3597>
 C. F. Tung  <https://orcid.org/0000-0001-6920-7841>
 M. A. Unland Elorrieta  <https://orcid.org/0000-0002-6124-3255>
 A. K. Upadhyay  <https://orcid.org/0000-0003-1957-2626>
 N. Valtonen-Mattila  <https://orcid.org/0000-0002-1830-098X>
 J. Vandenbroucke  <https://orcid.org/0000-0002-9867-6548>
 N. van Eijndhoven  <https://orcid.org/0000-0001-5558-3328>
 J. van Santen  <https://orcid.org/0000-0002-2412-9728>
 S. Verpoest  <https://orcid.org/0000-0002-3031-3206>
 C. Walck  <https://orcid.org/0000-0002-4188-9219>
 C. Weaver  <https://orcid.org/0000-0003-2385-2559>
 J. Weldert  <https://orcid.org/0000-0002-3709-2354>
 C. Wendt  <https://orcid.org/0000-0001-8076-8877>
 N. Whitehorn  <https://orcid.org/0000-0002-3157-0407>
 C. H. Wiebusch  <https://orcid.org/0000-0002-6418-3008>
 M. Wolf  <https://orcid.org/0000-0001-9991-3923>
 S. Yoshida  <https://orcid.org/0000-0003-2480-5105>
 T. Yuan  <https://orcid.org/0000-0002-7041-5872>
 Z. Zhang  <https://orcid.org/0000-0002-7347-283X>

References

- Aartsen, M., Ackermann, M., Adams, J., et al. 2020, *JInst*, 15, P06032
 Aartsen, M. G., Ackermann, M., Adams, J., et al. 2015, *ApJ*, 807, 46
 Aartsen, M. G., Ackermann, M., Adams, J., et al. 2017a, *JInst*, 12, P03012
 Aartsen, M. G., Ackermann, M., Adams, J., et al. 2017b, *Aph*, 92, 30
 Aartsen, M. G., Ackermann, M., Adams, J., et al. 2020, *PhRvL*, 124, 051103
 Aartsen, M. G., Ackermann, M., Adams, J., et al. 2018a, *Sci*, 361, 378
 Aartsen, M. G., Ackermann, M., Adams, J., et al. 2018b, *Sci*, 361, 147
 Abbasi, R., Abdou, Y., Abu-Zayyad, T., et al. 2011, *ApJ*, 732, 18
 Abbasi, R., Ackermann, M., Adams, J., et al. 2021a, *PhRvD*, 104, 022002
 Abbasi, R., Ackermann, M., Adams, J., et al. 2021b, arXiv:2101.09836
 Abbasi, R., Ackermann, M., Adams, J., et al. 2021c, *ApJL*, 920, L45
 Abbasi, R., Ackermann, M., Adams, J., et al. 2022a, *Sci*, 378, 538
 Abbasi, R., Ackermann, M., Adams, J., et al. 2022b, *ApJ*, 928, 50
 Abbasi, R., Ackermann, M., Adams, J., et al. 2023a, *ApJS*, 269, 25
 Abbasi, R., Ackermann, M., Adams, J., et al. 2023b, *ApJ*, 951, 45
 Abbasi, R., Ackermann, M., Adams, J., et al. 2021d, *ApJ*, 911, 67
 Abdo, A. A., Ackermann, M., Ajello, M., et al. 2010, *ApJS*, 188, 405
 Acero, F., Ackermann, M., Ajello, M., et al. 2015, *ApJS*, 218, 23
 Ackermann, M., Ajello, M., Albert, A., et al. 2012, *ApJS*, 203, 4
 Bartoli, B., Bernardini, P., Bi, X. J., et al. 2013, *A&A*, 551, A142
 Bianchi, L., Efremova, B., Herald, J., et al. 2011, *MNRAS*, 411, 2770
 Blaufuss, E., Kintscher, T., Lu, L., & Tung, C. F. 2019, *ICRC (Madison, WI)*, 358, 1021
 Boller, T., Freyberg, M. J., Trümper, J., et al. 2016, *A&A*, 588, A103
 Braun, J., Baker, M., Dumm, J., et al. 2010, *Aph*, 33, 175
 Braun, J., Dumm, J., De Palma, F., et al. 2008, *Aph*, 29, 299
 Condon, J. J., Cotton, W. D., Greisen, E. W., et al. 1998, *AJ*, 115, 1693
 D'Elia, V., Perri, M., Puccetti, S., et al. 2013, *A&A*, 551, A142
 Dempster, A. P., Laird, N. M., & Rubin, D. B. 1977, *J. R. Stat. Soc. Ser. B Methodol.*, 39, 1
 Eller, P., & Shtembari, L. 2023, *JInst*, 18, P03048
 Evans, P. A., Osborne, J. P., Beardmore, A. P., et al. 2014, *ApJS*, 210, 8
 Giommi, P., Arrigo, G., Barres De Almeida, U., et al. 2018, arXiv:1805.08505
 Gregory, P. C., Scott, W. K., Douglas, K., & Condon, J. J. 1996, *ApJS*, 103, 427
 Haack, C., & Wiebusch, C. 2017, *ICRC (Busan)*, 301, 1005
 Healey, S. E., Romani, R. W., Taylor, G. B., et al. 2007, *ApJS*, 171, 61
 Jackson, N., Battye, R. A., Browne, I. W. A., et al. 2007, *MNRAS*, 376, 371
 Karl, M. 2019, *ICRC (Madison, WI)*, 36, 929
 Karl, M., Abbasi, R., Ackermann, M., et al. 2023, *ICRC (Nagoya)*, 444, 974
 Karl, M., & Eller, P. 2023, arXiv:2312.15196
 Karl, M., Eller, P., & Schubert, A. 2021, *ICRC (Berlin)*, 37, 940
 Karl, M. S. 2022, Dissertation, Technische Univ. München, München <https://mediatum.ub.tum.de/node?id=1654955>
 Kintscher, T. 2016, *JPhCS*, 718, 062029
 Kronmueller, M., & Glauch, T. 2019, *ICRC (Madison, WI)*, 36, 937
 Myers, S. T., Jackson, N. J., Browne, I. W. A., et al. 2003, *MNRAS*, 341, 1
 Nieppola, E., Tornikoski, M., Lähteenmäki, A., et al. 2007, *AJ*, 133, 1947
 Nolan, P. L., Abdo, A. A., Ackermann, M., et al. 2012, *ApJS*, 199, 31
 Padovani, P., Giommi, P., Falomo, R., et al. 2022, *MNRAS*, 510, 2671
 Planck Collaboration, Ade, P. A. R., Aghanim, N., et al. 2011, *A&A*, 536, A7
 Planck Collaboration, Ade, P. A. R., Aghanim, N., et al. 2014, *A&A*, 571, A28
 Planck Collaboration, Ade, P. A. R., Aghanim, N., et al. 2016, *A&A*, 594, A26
 Voges, W., Aschenbach, B., Boller, T., et al. 1999, *A&A*, 349, 389
 Waxman, E., & Bahcall, J. N. 1999, *PhRvD*, 59, 023002
 White, R. L., & Becker, R. H. 1992, *ApJS*, 79, 331
 Wilks, S. S. 1938, *Ann. Math. Stat.*, 9, 60
 Wright, A. E., Griffith, M. R., Burke, B. F., & Ekers, R. D. 1994, *ApJS*, 91, 111
 Wright, E. L., Eisenhardt, P. R. M., Mainzer, A. K., et al. 2010, *AJ*, 140, 1868